

**POLYMER NANOCOMPOSITE MATERIALS WITH HIERARCHICAL FILLERS
AS A CONCEPTUAL FRAMEWORK FOR THE DESIGN OF
MULTIFUNCTIONAL MEMBRANES**

By

Christopher A. Crock

A THESIS

Submitted to
Michigan State University
In partial fulfillment of the requirements
for the degree of

MASTER OF SCIENCE

Environmental Engineering

2012

ABSTRACT

POLYMER NANOCOMPOSITE MATERIALS WITH HIERARCHICAL FILLERS AS A CONCEPTUAL FRAMEWORK FOR THE DESIGN OF MULTIFUNCTIONAL MEMBRANES

By

Christopher A. Crock

Since the isolation and discovery of graphene, researchers have sought to exploit its exceptional material properties for application in fields that range from electronics to polymer composites to medicine. Key publications on the synthesis, characterization and properties, and applications of graphene are reviewed in Chapter 1, as well as key publications on graphene-polymer nanocomposites as nonporous composites. In Chapter 2, graphene decorated with nanogold is investigated as a component of porous polymer nanocomposites for the bottom-up design of multifunctional membranes for water treatment. Nanogold decorated graphene, when incorporated into nanocomposite membranes, endows the membrane with catalytic functionality. The membrane reactivity was quantified using the catalytic reduction of 4-nitrophenol with nanogold as the catalyst. By using hierarchical nanostructures (i.e. graphene decorated nanogold), we showed that membrane structure (i.e. permeability, selectivity, and mechanical properties) and reactivity could be independently controlled, where structure depends on graphene content with 97.8% confidence and reactivity depends on nanogold surface area with 88.3% confidence.

Copyright by
CHRISTOPHER A. CROCK
2012

ACKNOWLEDGMENTS

To my family, thank you for your unconditional love and support. I would not be where I am without you.

To my advisor, Dr. Volodymyr Tarabara, thank you for guidance and support. Your encouragement, advice, and insight have been and will continue to be invaluable to my successes at Michigan State University.

To my committee members, Dr. Thomas Voice and Dr. Phanikumar Mantha, thank you for all your guidance.

To the former and current members of my research group at Michigan State University, thank you for your endless advice, thoughtful discussions, and positive attitudes both in and out of the lab.

To Lori Larner, Margaret Conner, Laura Taylor, Mary Mroz, Yanlyang Pan, and Joseph Nguyen, thank you for all your administrative and technical support.

TABLE OF CONTENTS

| | |
|---|------|
| LIST OF TABLES..... | viii |
| LIST OF FIGURES | ix |
| CHAPTER ONE | 1 |
| A review of graphene based nanomaterials and graphene-polymer nanocomposites | 1 |
| 1.1 Monolayer graphene sheets | 1 |
| 1.1.1 Properties of monolayer graphene | 4 |
| 1.1.2 Synthesis of monolayer graphene | 5 |
| 1.1.3 Application of monolayer graphene | 7 |
| 1.2 Graphite nanoplatelets | 9 |
| 1.2.1 Properties of graphite nanoplatelets..... | 9 |
| 1.2.2 Synthesis of graphite nanoplatelets | 12 |
| 1.2.3 Application of graphite nanoplatelets | 14 |
| 1.3 Graphene-polymer nanocomposites | 15 |
| 1.3.1 Benefits of graphene-polymer nanocomposites | 16 |
| 1.3.2 Current methods for the manufacture of graphene-polymer nanocomposites | 17 |
| References | 21 |
| CHAPTER TWO | 30 |
| Polymer nanocomposites with graphene-based hierarchical fillers as materials for multifunctional water treatment | 30 |
| 2.1 Introduction..... | 31 |
| 2.2 Approach..... | 34 |
| 2.3 Experimental | 39 |
| 2.3.1 Reagents..... | 39 |
| 2.3.2 Preparation and characterization of Au-xGnP nanoparticles..... | 39 |
| 2.3.3 Membrane preparation | 40 |
| 2.3.3.1 Preparation of polysulfone membranes | 41 |
| 2.3.3.2 Preparation of nanocomposite membranes | 43 |
| 2.3.4 Membrane characterization..... | 44 |
| 2.3.4.1 Membrane permeability and molecular weight cutoff..... | 44 |
| 2.3.4.2 Mechanical properties | 45 |
| 2.3.4.3 Catalyst content of nanocomposite membranes..... | 46 |
| 2.3.4.4 Catalytic activity..... | 47 |
| 2.3.4.5 SEM and TEM imaging..... | 49 |
| 2.4 Results and discussion..... | 50 |
| 2.4.1 Properties of Au-xGnP nanoparticles | 50 |
| 2.4.2 Morphology of nanocomposite membranes | 53 |
| 2.4.3 Permeability and selectivity of nanocomposite membranes | 59 |
| 2.4.4 Mechanical properties of nanocomposite membranes | 62 |

| | |
|---|----|
| 2.4.5 Transient behavior of membrane permeability: apparent compaction resistance of xGnP/PSf membranes | 64 |
| 2.4.6 Catalytic activity of nanocomposite membranes | 67 |
| 2.4.7 Independent control of membrane's structure and additional functions..... | 71 |
| 2.4.8 Analysis of statistical significance on the independent control of membrane structure and additional functions..... | 75 |
| 2.4.9 Practicability and environmental implications | 77 |
| 2.5 Conclusions..... | 80 |
| Acknowledgments | 81 |
| Supporting documentation | 82 |
| Appendix | 93 |
| References..... | 96 |

LIST OF TABLES

| | |
|---|----|
| Table 1: Composition of membrane casting mixtures for polysulfone membranes (controls) and for nanocomposite membranes with different loadings of xGnP and Au-xGnP. | 41 |
| Table 2: Confidence-levels of the reactive flux ($k_{obs} \cdot l_{eff}$) and permeability dependence on either both xGnP/PSf and Au/PSf loadings (A and B), or only Au/PSf (C) or xGnP/PSf (D) loadings..... | 76 |
| Table 3: The average rejection of dextrans with molecular weights, 5, 12, 25, 80, and 150 kDa are recorded in the table with the corresponding 90% confidence interval. | 87 |

LIST OF FIGURES

| | |
|--|----|
| Figure 1: Returned search results from ISI Web of Science for the search terms "graphene" and "graphene + composite" on a per year basis..... | 3 |
| Figure 2: A conceptual illustration of different forms of graphite and their corresponding interspatial thicknesses. | 11 |
| Figure 3: Conceptual illustration of hierarchical nanofillers as building blocks for multifunctional nanocomposite membranes..... | 34 |
| Figure 4: Filler content of nanocomposite membranes (denoted as B, C, C*, D, and D*) evaluated in this study. Filler-free polysulfone membrane (denoted A) is indicated as a reference. $xGnP_{total}$ denotes the mass of embedded xGnP originating from both non-decorated xGnPs and Au-decorated xGnPs. See Table 1 for the detailed composition of each membrane. | 36 |
| Figure 5: SEM (A, B) and TEM (C, D) micrographs of xGnPs (A) and xGnPs decorated by gold nanoparticles (C, D). Figure D is a magnified view of a portion of the platelet shown in Fig. C..... | 51 |
| Figure 6: Photographs of membranes with different xGnP loading..... | 53 |
| Figure 7: SEM micrographs of membrane skin (top row) and membrane cross-sections (middle row) for a) neat PSf, b) 0.1% xGnP/PSf, c) 1.0% xGnP/PSf, and d) 2.0% xGnP/PSf membranes. The trends in macrovoid morphology as a function of xGnP loading are schematically illustrated in the bottom row. | 55 |
| Figure 8: SEM micrographs of xGnPs embedded within the dense top-layer (top, middle) and macrovoid (bottom) regions of xGnP/PSf and Au-xGnP/PSf membranes..... | 57 |
| Figure 9: Rejection of 12 kDa dextran and pure water permeability of xGnP/PSf and Au-xGnP/PSf membranes as functions of xGnP loading. The permeability of xGnP-free PSf membranes is $1.3 \pm 1.1 \text{ L}/(\text{m}^2 \cdot \text{h} \cdot \text{bar})$. Error bars correspond to 90% confidence level. | 60 |
| Figure 10: Tensile strength and % elongation of membrane specimens as functions of xGnP loading. Error bars correspond to 90% confidence interval. | 62 |
| Figure 11: Compaction behavior of neat PSf membranes (-□-) and PSf nanocomposite membranes filled with 1 wt% of xGnP or Au-xGnP (-□-) under the applied transmembrane pressure of 20 psi (1.38 bar). | 65 |
| Figure 12: Observed reaction rate constant as a function of Au/PSf loading. Error bars correspond to the 90% confidence interval. | 69 |

| | |
|--|----|
| Figure 13: Reduction of 4-nitrophenol as a function of permeate flux for membranes with different Au-xGnP/PSf and (Au-xGnP + xGnP)/PSf loadings. | 72 |
| Figure 14: Reduction of 4-nitrophenol normalized by Au content in mg as a function of permeate flux for membranes with different Au-xGnP/PSf and (Au-xGnP + xGnP)/PSf loadings..... | 73 |
| Figure 15: Schematic of experimental setup for permeability and catalytic measurements. | 83 |
| Figure 16: Permeate flux and 4-NP reduction as a function of time. | 84 |
| Figure 17: The figure shows an example fit as a pseudo plug reactor in the first order. For each flux four measurements of 4-nitrophenol reduction were used, and the red dashed line represents the 90% confidence interval of the fit..... | 85 |
| Figure 18: A schematic showing how the cast nanocomposite membrane was apportioned for specific characterization experiments. | 86 |
| Figure 19: SEM micrographs of aggregated nanogold. The image was obtained using the backscatter electron detector (a) and secondary electron detector (b) | 88 |
| Figure 20: Backscatter SEM micrograph of Au-xGnP. | 89 |
| Figure 21: X-ray diffraction spectrum of Au-xGnP diffraction peaks corresponding to Au and C..... | 90 |
| Figure 22: The figure of merit is calculated as permeability, $L/(m^2 \cdot h \cdot bar) \times 12$ kDa rejection, % and is plotted as a function of xGnP/PSf loading. | 91 |

CHAPTER ONE

A review of graphene based nanomaterials and graphene-polymer nanocomposites

Sections 1.1 and 1.2 review the characterization and properties, synthesis, and application of monolayer graphene sheets and graphite nanoplatelets (GNPs), respectively. Section 1.3 reviews key publications on non-porous graphene-polymer nanocomposites.

1.1 Monolayer graphene sheets

Graphene is a single layer of sp^2 bonded carbon atoms that displays exceptional mechanical, electrical, optical, and thermal properties – all of which continue to give graphene the attention of researchers in various areas of study. A single layer of atoms, or atomic plane, is the building block of bulk crystals, as is the case with bulk graphite consisting of graphene sheets. It was believed that 2D materials, like graphene, could not exist because they were too unstable unless supported by a 3D structure. Both theoretical calculations and experimental observations showed that 2D materials were unstable in such low dimensional systems due to atomic displacements caused by thermal fluctuations [1][2]. When compared to multi and single walled nanotubes, theoretical calculations using the reactive empirical bond-order potential show that monolayer and

multilayer graphene were the most unstable until approximately 6000 atoms in thickness (about 20 nm), but when the structure was larger than 24,000 atoms in thickness (i.e. graphite) it became the most stable structure [3]. Despite all doubts, in 2004, in a simple but ingenious experiment, Andre Geim and Konstantin Novoselov isolated the 2D structure, graphene. They mechanically exfoliated graphite, the 3D system of layered graphene, by repeatedly peeling off layers from graphite simply using scotch tape, not unlike lifting a fingerprint, until the graphene was isolated [2]. Since the discovery and isolation of graphene, the number of graphene-related publications has grown exponentially [4] (**Figure 1**).

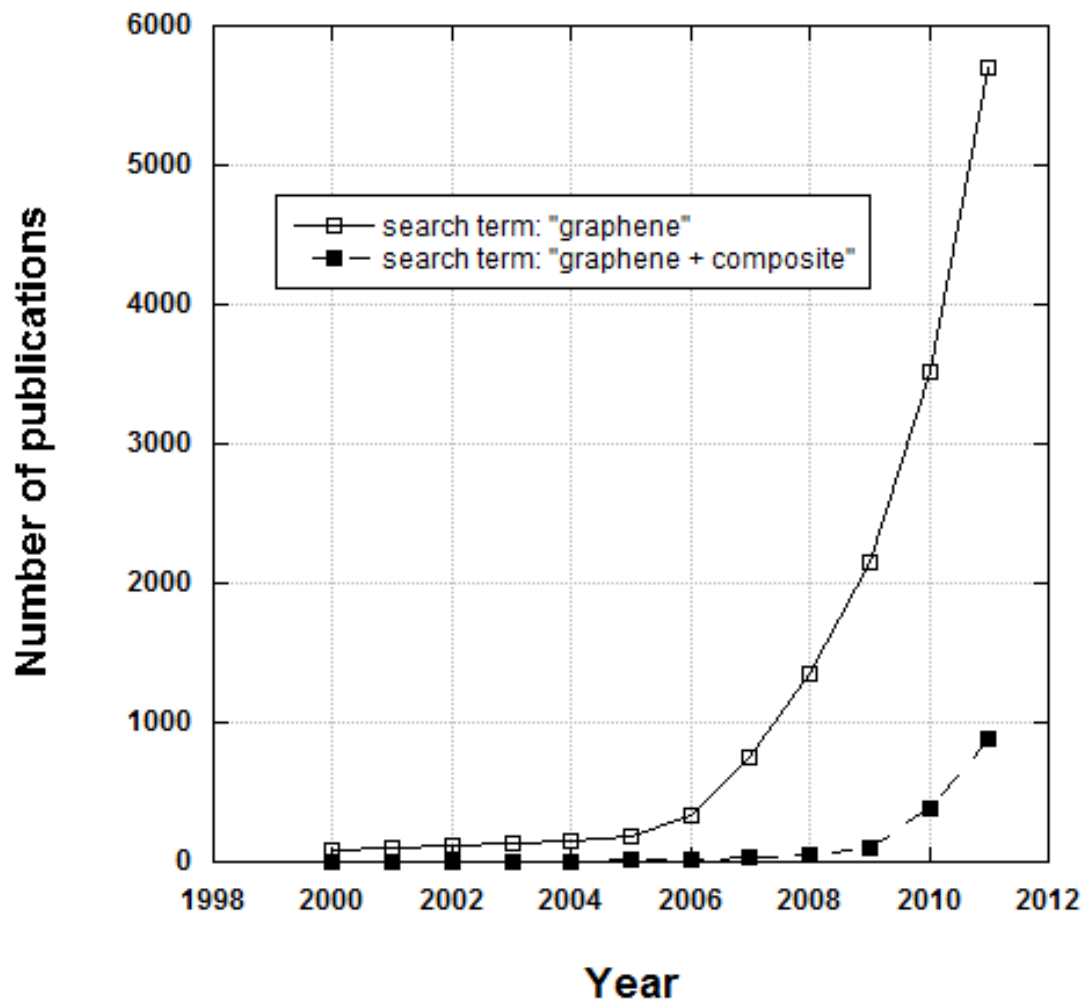


Figure 1: Returned search results from ISI Web of Science for the search terms "graphene" and "graphene + composite" on a per year basis.

1.1.1 Properties of monolayer graphene

To quote Andrei Geim, “Graphene is an ultimate incarnation of the surface: It has two faces with no bulk left in between” [5], and this surface has remained relatively unexplored. What is well known is that the basal plane of graphene can readily adsorb and desorb various atoms and molecules. Donor and acceptor adsorbates lead to changes mostly in charge carrier concentration, allowing for graphene to remain highly conductive, but certain adsorbates such as H^+ and OH^- create local states near the neutral charge point that limit the mean free path for the carrier (vacancies also limit the mean free path) [6]. The limited paths are caused by defects in the sp^2 hybridization and give rise to poorly conductive graphene [7][8]. Graphene sheets with oxygen containing adsorbates (i.e. graphene oxide or GO), such as hydroxyl and epoxide groups, are less likely to restack and aggregate due to the repulsion by functional groups at the basal plane. GO is also hydrophilic and, as a result, can be easily dispersed in water [8][9]. It is possible to nearly return GO to its original electronic structure by reducing graphene either through thermal annealing (~ 1000 °C) or by using reducing agents such as hydrazine [10–12], sodium borohydride [13][14], or hydroquinone gaseous hydrogen [15] to reduce all oxygen containing groups.

Graphene also has superior mechanical properties. The thermal conductivity for graphene was recorded as $5,000 \text{ W m}^{-1} \text{ K}^{-1}$ [16] (compared with copper near

$400 \text{ W m}^{-1} \text{ K}^{-1}$) and Young's modulus as 1.0 TPa [17] (compared with steel near 0.2 TPa). Also, it was measured that graphene could be stretched 20% more than any other crystal [17][18]. An unparalleled feature of graphene that is intriguing to many researchers is the observation that graphene has an extremely low permeability to most gasses [19]; however, water vapor was transported across a thin film of stacked graphene sheets at rates 10 orders of magnitude higher than He [20]. Some of the basic physical properties of graphene remain unknown, such as the melting and phase transition temperature.

1.1.2 Synthesis of monolayer graphene

Since graphene was first isolated by micro-mechanically exfoliating graphite using scotch tape to pull layers of graphene from bulk graphite, micro-mechanical exfoliation continues to be a method to synthesize monolayer graphene.

Because aggregation impedes the bulk production of graphene [21], individual graphene sheets must be well separated, lest irreversible stacking due to van der Waals forces occurs. To prevent aggregation, graphite can be oxidized before micro-mechanical exfoliation [22][23]. However, the intense chemical oxidation of graphene results in structural defects that make it difficult to fully regenerate the original electronic structure that it once had, as shown by Raman spectroscopy [7][10]. Because structural defects generate the loss of electronic properties during oxidative treatment, this synthesis approach is more desirable when only the geometric structure of graphene needs to be maintained. It has been shown

that graphite can be exfoliated via sonication in solvents that have similar surface energies as graphene, such as N-methyl-pyrrolidone, to produce defect-free graphene [24][25]. The use of surfactants such as sodium dodecylbenzene sulfonate and sodium cholate [25] was shown to help stabilize graphene sheets via Coulombic repulsion of the surfactant-coated sheets during exfoliation.

Rather than using harsh oxidative treatments followed by micro-mechanical exfoliation, graphite can be expanded by the intercalation of small molecules in between layers of graphite and exfoliated using micro-mechanical or thermal methods to produce monolayer graphene [22][23][27]. By incorporating small molecules that do not covalently bond with graphene, graphite can be expanded while the electronic structure remains unaltered and often improved. This is not the case for molecules that are covalently bonded to the graphene because of the disruption to the sp^2 hybridization. After expansion, graphite can then be dispersed and exfoliated in solvents such as N,N-dimethylformamide [28] to produce monolayer graphene sheets, obviating the need to first oxidize or functionalize the graphite.

Chemical vapor deposition (CVD) is another route for monolayer graphene synthesis and shows the most promise for large-scale production of monolayer graphene sheets or thin-films that could be used in the electronics industry [29][30]. One mechanism for monolayer graphene formation involves the diffusion and subsequent precipitation of carbon in a metal substrate that has

moderately high carbon solubility as shown by Somani et al [30]. Using a low solubility metal substrate (e.g. Cu) in a methane saturated environment, the nucleation and subsequent growth of monolayer graphene islands at C_xH_y supersaturated sites on the substrate can be used to synthesize monolayer graphene sheets and thin-films [29]. In 2006, Somani et al. showed the first successful CVD of few layer graphene films on high carbon solubility Ni using the precursor, camphor [30]. By using the CVD route, new control parameters for regulating the graphene structure became available – folding can be minimized [31][32], the number of graphene layers can be controlled [29][33][34], and doping is possible (e.g. [35]). Finally, SiC substrates can be thermally decomposed to monolayer graphene sheets on the surface of the SiC substrate [36–38]. The SiC substrate is heated under an ultrahigh vacuum, and the Si atoms sublime from the substrate, leaving C atoms to rearrange forming graphene sheets on the surface.

1.1.3 Application of monolayer graphene

There is a wide array of applications for graphene, however, electronics and polymer nanocomposites are two application areas that are discussed here. Graphene's electronic and optical properties can be taken advantage of in computer electronics, and its mechanical properties make it an exceptional material for use in thin films.

Because different forms of graphene have different electrical properties – pristine graphene is very conductive and GO can be semi- or non-conductive – an all graphene circuit can be envisaged [5]. As an electron-accepting material, graphene was shown to be a competitive alternative to the fullerene derived electron acceptor for photovoltaic devices [39]. Due to its high thermal conductivity, graphene shows promise as a material for thermal management on Si/SiO₂ circuits in nanoelectronics [40]. Graphene sheets grown on a Ni substrate were used to construct ultra-capacitors that operated in a wider voltage range than that afforded by current aluminum electrolyte capacitor technology [41].

Functionalized graphene has potential in thin-film based materials because of its superior mechanical properties [20][42][43]. In the form of thin-films, functionalized graphene is highly flexible and mechanically robust [44]. The extremely low permeability of individual graphene sheets to most gasses, functionalized graphene films could be developed for separation and transport processes (e.g. filtration, (bio)molecular, and ion transport). The structure of graphene, specifically the extent of graphene corrugation, can be controlled to regulate separation properties of thin multilayer graphene films with respect to nanoparticles [45]. Reduced GO was used to fabricate transparent thin films that were electrically conductive, and have potential application for transparent electrodes [33].

1.2 Graphite nanoplatelets

1.2.1 Properties of graphite nanoplatelets (GNPs)

Graphite nanoplatelets (GNPs), ideally, are stacked single-layered graphene sheets that are held together via weak van der Waals forces between individual graphene sheets. The interspatial thickness for stacked graphene sheets in pristine graphite is 0.34 nm; therefore, the thickness of graphite nanoplatelets ranges from 0.34 nm for a bilayer of graphene to ≤ 100 nm for up to 294 layers of stacked graphene [46] (see **Figure 2**). The interlayer spacing for stacked sheets of GO is greater because of the presence of functional groups at the basal plane. The spacing also depends on the local conditions. In a high vacuum, the interlayer spacing is 0.6 nm, but at 45% relative humidity it is 0.8 nm because of the intercalation of water [47][48]. Just as monolayer graphene exhibits unique characteristics, multi-layer graphene (i.e. GNPs) also exhibits unique physical, chemical, and mechanical properties [43][49–51]. In the following discussion, the collective nanoparticle of stacked graphene platelets is referred to as a graphite nanoplatelet; however, when discussing the planar graphene derivatives of GNPs, the nanoparticle is referred to as monolayer graphene.

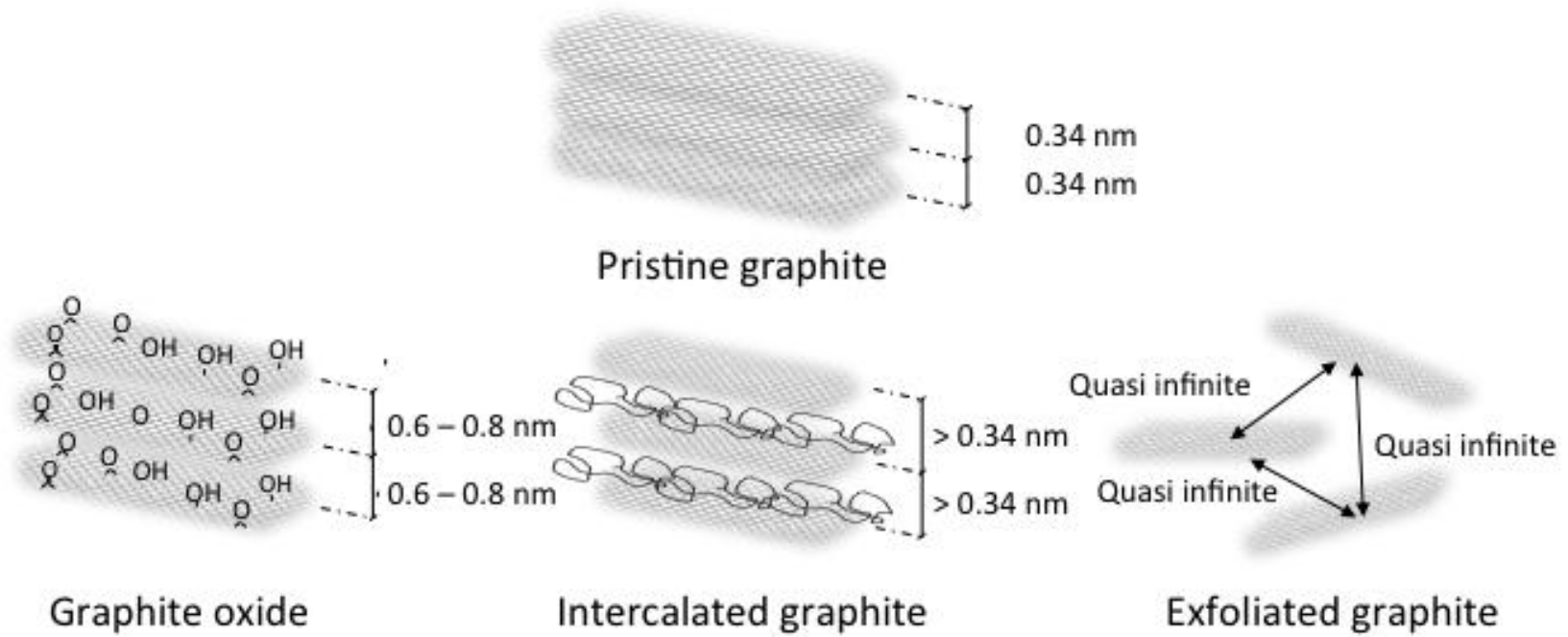


Figure 2: A conceptual illustration of different forms of graphite and their corresponding interspatial thicknesses.

1.2.2 Synthesis of GNPs

Prior to the discovery or isolation of monolayer graphene, researchers attempted to manufacture GNPs or thin graphite flakes as they were first described. In 1988, samples produced in these studies were stacked monolayer graphene flakes that were generally greater than 100 nm in thickness with some flakes as thin as 10 nm [52]. The intercalation of strong acids followed by thermal expansion and then micro-mechanical exfoliation was used to produce thin graphite flakes; presently, it is this approach that is mainly used to produce graphite oxide [53].

GNPs can be manufactured using two conceptually distinct methodologies – the top-down approach and the bottom-up approach. For both methods multiple routes exist for the manufacture of GNPs. The top-down approach essentially separates bulk graphite to GNPs of lower dimensionality. The “scotch tape” method used by Geim and Novoselov to produce monolayer graphene was a top-down approach. Mechanical exfoliation can be used to produce high quality GNPs with high aspect ratios. xGnPs[®] is a commercially produced GNP product prepared using pristine graphite as the source material. To make xGnPs, graphite is intercalated with acid, expanded by rapid heating, and then pulverized to exfoliate the expanded graphite into GNPs of specific dimensions [55]. These nanoplatelets range from approximately 2 × 2 μm to 15 × 15 μm in diameter with thicknesses of approximately 2 to 12 nm. Pristine graphite fine powder can also

be directly exfoliated by sonication to solubilized GNPs in the following solvents: hexafluorobenzene, octafluorotoluene, pentafluorobenzonitrile, pentafluoronitrobenzene, pentafluoropyridine, and pyridine [54].

Another promising route for the production of GNPs via the top down approach involves starting with graphite oxide rather than pristine graphite. While GO is similar to graphite in that it is made up of stacked graphene sheets, the functional groups and surface defects change the mechanical, thermal, and electrical properties of the graphene sheets. Due to the increased interlayer spacing though, graphite oxide can easily be intercalated with various molecules and subsequently exfoliated. Graphite oxide has been exfoliated by first intercalating monomers between the layers followed by in situ polymerization [56]. Rapidly heating graphite oxide at high temperatures (~ 1000 °C) also exfoliates GNPs, and, in addition, reduces the graphite oxide [57]. Exfoliation by thermal means results from the pressure of CO_2 generated by the decomposition of hydroxyl and epoxy sites at the basal planes of stacked graphene sheets. The GNPs resulting from graphite oxide precursors can be reduced either thermally, as mentioned above, or chemically. The chemical reduction of oxidized GNPs is similar to the reduction of monolayer GO as described in section 1.1.1 by using hydrazine [10–12], sodium borohydride [13][14] hydroquinone gaseous hydrogen [15], and UV irradiated TiO_2 [58].

Bottom-up approaches are those that stack or build on few layer GNPs or

monolayer graphene sheets to produce thicker GNPs. CVD and the decomposition of SiC substrates are two routes for producing high-quality monolayer and few layer GNPs as described in section 1.1.2. The disadvantage of this approach, however, is the inherent need for a support for deposition and growth. Despite this disadvantage, using CVD [29][32–34][59] and SiC decomposition [36–38] may be a viable route of GNP production for the electronic industry because the electronics industry already uses Si substrates for circuit printing. It would not, however, be viable for the mass production of GNPs as a material for polymer nanocomposites. The filtration of monolayer graphene dispersed in solvents can also produce high quality stacked graphene composites as thin films [20][43][45][60]. Using the filtration route, however, does not produce the discrete GNPs that the other described routes produce, but the thin films that result continue to display exceptional electrical, thermal, and optical properties of discrete GNPs.

1.2.3 Application of GNPs

GNPs have been extensively used as filler material in the preparation of polymer nanocomposites. As fillers, GNPs offer several advantages including processability and ability to enhance mechanical, thermal, and electrical properties of the nanocomposites (see section 1.3.1).

The extremely high surface area (up to 2,600 m²/g for monolayer graphene), thermal stability, and electronic properties of GNPs make these materials desirable supports for nanoparticles carrying specific functions (e.g. catalytic, sensing, and magnetic) to endow the polymer nanocomposite with these useful functionalities. GNPs decorated with bimetallic Pt-Co and Pt-Cr nanocatalysts were used to improve the electrocatalytic activity in fuel cells [61]. Both Pt and Pd decorated and undecorated GNPs were used as a glucose biosensor showing rapid response times for detection in Nafion-water-isopropyl alcohol solution [49], [62]. Pd decorated GNPs were used as highly active catalysts for cross-coupling reactions, specifically the Suzuki and Heck C-C coupling reaction [63]. Decorated GNPs have also been suggested for use in solar cells to improve performance [64].

1.3 Graphene-polymer nanocomposites

Polymer organo-clay composites were one of the first classes of polymer nanocomposites, and they were proclaimed as a new class of materials that promoted greater control of materials for specific applications [65]. To the best of our knowledge, all graphene-polymer nanocomposite studies published to-date have been on non-porous composites. The present study and the earlier work in our group that this study builds on [66] are the first to focus on porous graphene-polymer composites (see Chapter 2).

1.3.1 Beneficial properties of graphene-polymer nanocomposites

Monolayer graphene and GNPs can be components of polymer nanocomposites and are of special interest because of graphene's intrinsic properties (see section 1.1) that can potentially be inherited by polymer nanocomposites [21][51][67].

The application of graphene-polymer nanocomposites faces challenges both in the manufacture of the graphene composite and in understanding polymer-graphene interactions in the and how they affect nanocomposite's properties.

Generally, GNPs that are aligned and/or have higher aspect ratios (i. e. GNPs with few layers) in a polymer matrix display stronger influence on the electrical, thermal, and mechanical properties of the polymer nanocomposite [68–70]. For aligned and high aspect ratio GNPs, both the electrical conductivity and material strength were greater than polyurethane nanocomposites where nanofillers had smaller aspect ratios and were not aligned [68]. Highly anisotropic and GNPs of few layers show that thermal conductivity increased to values as high as $80 \text{ W m}^{-1} \text{ K}^{-1}$ for epoxy polymer nanocomposites [69], where the previous record for thermal conductivity was $7 \text{ W m}^{-1} \text{ K}^{-1}$. Aligned GNPs with high aspect ratios used in crystalline polymer nanocomposites show a 25% over 16% improvement in the mechanical modulus for randomly oriented GNPs [70].

There is strong evidence that addition of graphene to a polymer alters its glass transition temperature (T_g). Substantial evidence explains the change by the

restriction of polymer chain mobility at the interface of graphene-polymer; therefore, the interaction between nanofiller and polymer is extremely important [71–73]. For GNPs dispersed in polymer matrices using non-covalent methods, low loadings of nanofiller show significant increases in T_g [42], but for GNPs dispersed by covalent methods both significant increases [74] and decreases [75] were observed. Glass transition temperatures are important in polymer nanocomposites because they provide fundamental insights to the polymer chain mobility in the presence of graphene nanofillers [42].

1.3.2 Current methods for the manufacture of graphene-polymer nanocomposites

The manufacture of graphene-polymer nanocomposites requires controlled dispersion of the graphene-based nanofiller without aggregation. There are multiple routes for dispersing graphene-based materials in polymer matrices, and the routes can be split into two subcategories – those that rely on non-covalent bonding between graphene and the polymer and those that rely on covalent bonding.

Methods relying on non-covalent bonding include solution mixing, melt mixing, and in-situ polymerization. Solution mixing involves either mixing agglomerates of graphene-based nanofillers with polymer (the polymer can be dissolved prior to or during the addition of the nanofiller) or mixing well dispersed graphene nanofillers in a solvent with a polymer. The polymer nanocomposite solution can

then be processed into the final product by wet, dry, or thermal phase inversion methods or a combination thereof. Solution mixing has been used to incorporate graphene-based nanofillers in various polymers, such as polysulfone (see Chapter 2), polystyrene [51], polycarbonate [76], polyimides [77], poly (methyl methacrylate) [42], poly(vinyl alcohol) (PVA) [78], and poly(allylamine) (PAA) [79]. Water soluble polymers such as PVA and PAA are appealing because thin-film nanocomposites can be produced simply by filtering a solution of the polymer and highly dispersed GNPs [20][80]. Aggregation (i.e. restacking) may still occur during solution mixing, but it can be prevented by treating the nanofiller to increase its levels of exfoliation or functionalization (see Sections 1.1.2 and 1.2.2) prior to or during mixing. Melt mixing involves mixing powder form polymer and graphene-based nanofiller agglomerates under high shear and heat conditions to form a polymer nanocomposite solution. The benefit of melt mixing versus solution mixing is that a solvent is not required; however, evidence shows that melt mixing cannot achieve as high dispersion levels as solution mixing [68][81]. The most notable drawback is that, to date, dispersing single or few layer GNPs during melt mixing has been unsuccessful. In situ polymerization requires the mixing of graphene-based nanofillers with a monomer solution followed by polymerization of the monomers. Monomers intercalate graphene layers in graphite (e.g. expanded graphite, exfoliated graphite, or graphite oxide) and a polymerization step exfoliates the graphite to GNPs of few layers. Expanded graphite was exfoliated to few layer GNPs and intercalated with poly(ethylene), which subsequently underwent polymerization to form graphene-

polymer nanocomposites [82]. PMMA was used to intercalate the galleries of GO and was polymerized to produce exfoliated GNPs that were well dispersed in a PMMA matrix [83]. Poly(pyrrole) was polymerized in GO galleries to form graphene-polymer nanocomposites that had a conductivity four orders of magnitude higher than pristine GO [56]. It should be noted that the polymer and graphene were not covalently bonded in situ polymerization studies cited above, but this method is also used in dispersion methods that rely on covalent bonding.

For dispersion methods involving covalent bond formation, polymers are either grafted to or grown from the graphene surface. Because GO is rich in reactive surface functional groups, it is a promising form of graphene to be used in this method. Atom transfer radical polymerization (ATRP) initiators can be used in the “growing from” approach. ATRP allows for controlled polymerization where molecular weight and architecture of the polymer can be controlled as determined by the initiator. GO was functionalized with an ATRP initiator, and the monomers (styrene, methyl methacrylate, and tris(2-aminoethyl)amine) underwent polymerization forming polymer brushes with high degree of control from the GO surface [84]. Two examples of the “grafted to” approach are polystyrene terminated with azide grafted to GO nanoplatelets using Cu catalyst [85], and PVA grafted to GO nanoplatelets by esterification [86].

Graphene-based fillers can enhance mechanical, electrical, thermal, and optical properties of polymer nanocomposites. The questions of how the nanofiller

interacts with the matrix polymer and affects nanocomposite formation process are of key importance for the rational design these materials. Two challenges currently being addressed are developing methods of dispersing graphene-based fillers in polymer nanocomposites and understanding the fundamental properties of graphene and how it interacts with the various matrix polymers in nanocomposites.

REFERENCES

REFERENCES

- [1] A. K. Geim and K. S. Novoselov, "The rise of graphene," *Nature Materials*, vol. 6, no. 3, pp. 183–191, 2007.
- [2] K. S. Novoselov, A. K. Geim, S. V. Morozov, D. Jiang, Y. Zhang, S. V. Dubonos, I. V. Grigorieva, and A. A. Firsov, "Electric Field Effect in Atomically Thin Carbon Films," *Science*, vol. 306, no. 5696, pp. 666–669, Oct. 2004.
- [3] S. B. Sinnott, R. Andrews, D. Qian, A. M. Rao, Z. Mao, E. C. Dickey, and F. Derbyshire, "Model of carbon nanotube growth through chemical vapor deposition," *Chemical Physics Letters*, vol. 315, no. 1, pp. 25–30, 1999.
- [4] A. Barth and W. Marx, "Graphene - A rising star in view of scientometrics," Aug. 2008.
- [5] A. K. Geim, "Graphene: Status and Prospects," *Science*, vol. 324, no. 5934, pp. 1530–1534, Jun. 2009.
- [6] J.-H. Chen, W. Cullen, C. Jang, M. Fuhrer, and E. Williams, "Defect Scattering in Graphene," *Physical Review Letters*, vol. 102, no. 23, Jun. 2009.
- [7] S. Stankovich, D. A. Dikin, R. D. Piner, K. A. Kohlhaas, A. Kleinhammes, Y. Jia, Y. Wu, S. T. Nguyen, and R. S. Ruoff, "Synthesis of graphene-based nanosheets via chemical reduction of exfoliated graphite oxide," *Carbon*, vol. 45, no. 7, pp. 1558–1565, Jun. 2007.
- [8] S. Stankovich, R. D. Piner, X. Chen, N. Wu, S. T. Nguyen, and R. S. Ruoff, "Stable aqueous dispersions of graphitic nanoplatelets via the reduction of exfoliated graphite oxide in the presence of poly(sodium 4-styrenesulfonate)," *Journal of Materials Chemistry*, vol. 16, no. 2, p. 155, 2006.
- [9] D. Li, M. B. Müller, S. Gilje, R. B. Kaner, and G. G. Wallace, "Processable aqueous dispersions of graphene nanosheets," *Nature Nanotechnology*, vol. 3, no. 2, pp. 101–105, 2008.
- [10] G. Eda, G. Fanchini, and M. Chhowalla, "Large-area ultrathin films of reduced graphene oxide as a transparent and flexible electronic material," *Nature Nanotechnology*, vol. 3, no. 5, pp. 270–274, 2008.
- [11] H. A. Becerril, J. Mao, Z. Liu, R. M. Stoltenberg, Z. Bao, and Y. Chen, "Evaluation of Solution-Processed Reduced Graphene Oxide Films as Transparent Conductors," *ACS Nano*, vol. 2, no. 3, pp. 463–470, Mar. 2008.
- [12] C. Gómez-Navarro, R. T. Weitz, A. M. Bittner, M. Scolari, A. Mews, M. Burghard, and K. Kern, "Electronic Transport Properties of Individual Chemically Reduced Graphene Oxide Sheets," *Nano Lett.*, vol. 9, no. 5, p. 2206, 2009.

- [13] A. B. Bourlinos, D. Gournis, D. Petridis, T. Szabó, A. Szeri, and I. Dékány, "Graphite Oxide: Chemical Reduction to Graphite and Surface Modification with Primary Aliphatic Amines and Amino Acids," *Langmuir*, vol. 19, no. 15, pp. 6050–6055, Jul. 2003.
- [14] H.-J. Shin, K. K. Kim, A. Benayad, S.-M. Yoon, H. K. Park, I.-S. Jung, M. H. Jin, H.-K. Jeong, J. M. Kim, J.-Y. Choi, and Y. H. Lee, "Efficient Reduction of Graphite Oxide by Sodium Borohydride and Its Effect on Electrical Conductance," *Advanced Functional Materials*, vol. 19, no. 12, pp. 1987–1992, 2009.
- [15] S. Wang, P.-J. Chia, L.-L. Chua, L.-H. Zhao, R.-Q. Png, S. Sivaramakrishnan, M. Zhou, R. G.-S. Goh, R. H. Friend, A. T.-S. Wee, and P. K.-H. Ho, "Band-like Transport in Surface-Functionalized Highly Solution-Processable Graphene Nanosheets," *Advanced Materials*, vol. 20, no. 18, pp. 3440–3446, 2008.
- [16] A. A. Balandin, S. Ghosh, W. Bao, I. Calizo, D. Teweldebrhan, F. Miao, and C. N. Lau, "Superior Thermal Conductivity of Single-Layer Graphene," *Nano Lett.*, vol. 8, no. 3, pp. 902–907, 2008.
- [17] C. Lee, X. Wei, J. W. Kysar, and J. Hone, "Measurement of the elastic properties and intrinsic strength of monolayer graphene," *Science*, vol. 321, no. 5887, pp. 385–388, Jul. 2008.
- [18] V. Pereira, A. Castro Neto, and N. Peres, "Tight-binding approach to uniaxial strain in graphene," *Physical Review B*, vol. 80, no. 4, Jul. 2009.
- [19] J. S. Bunch, S. S. Verbridge, J. S. Alden, A. M. van der Zande, J. M. Parpia, H. G. Craighead, and P. L. McEuen, "Impermeable Atomic Membranes from Graphene Sheets," *Nano Letters*, vol. 8, no. 8, pp. 2458–2462, Aug. 2008.
- [20] R. R. Nair, H. A. Wu, P. N. Jayaram, I. V. Grigorieva, and A. K. Geim, "Unimpeded Permeation of Water Through Helium-Leak-Tight Graphene-Based Membranes," *Science*, vol. 335, no. 6067, pp. 442–444, Jan. 2012.
- [21] V. Singh, D. Joung, L. Zhai, S. Das, S. I. Khondaker, and S. Seal, "Graphene based materials: Past, present and future," *Progress in Materials Science*, vol. 56, no. 8, pp. 1178–1271, Oct. 2011.
- [22] F. Kang, Y. Leng, and T.-Y. Zhang, "Influences of H₂O₂ on synthesis of H₂SO₄-GICs," *Journal of Physics and Chemistry of Solids*, vol. 57, no. 6–8, pp. 889–892, Jun. 1996.
- [23] F. Kang, T.-Y. Zhang, and Y. Leng, "Electrochemical behavior of graphite in electrolyte of sulfuric and acetic acid," *Carbon*, vol. 35, no. 8, pp. 1167–1173, 1997.
- [24] Y. Hernandez, V. Nicolosi, M. Lotya, F. M. Blighe, Z. Sun, S. De, I. T. McGovern, B. Holland, M. Byrne, Y. K. Gun'Ko, J. J. Boland, P. Niraj, G. Duesberg, S. Krishnamurthy, R. Goodhue, J. Hutchison, V. Scardaci, A. C. Ferrari, and J. N. Coleman, "High-yield production of graphene by liquid-

phase exfoliation of graphite,” *Nature Nanotechnology*, vol. 3, no. 9, pp. 563–568, 2008.

- [25] P. Blake, P. D. Brimicombe, R. R. Nair, T. J. Booth, D. Jiang, F. Schedin, L. A. Ponomarenko, S. V. Morozov, H. F. Gleeson, E. W. Hill, A. K. Geim, and K. S. Novoselov, “Graphene-Based Liquid Crystal Device,” *Nano Letters*, vol. 8, no. 6, pp. 1704–1708, Jun. 2008.
- [26] M. Lotya, Y. Hernandez, P. J. King, R. J. Smith, V. Nicolosi, L. S. Karlsson, F. M. Blighe, S. De, Z. Wang, I. T. McGovern, G. S. Duesberg, and J. N. Coleman, “Liquid Phase Production of Graphene by Exfoliation of Graphite in Surfactant/Water Solutions,” *Journal of the American Chemical Society*, vol. 131, no. 10, pp. 3611–3620, Mar. 2009.
- [27] Y.-X. Pan, Z.-Z. Yu, Y.-C. Ou, and G.-H. Hu, “A new process of fabricating electrically conducting nylon 6/graphite nanocomposites via intercalation polymerization,” *Journal of Polymer Science Part B: Polymer Physics*, vol. 38, no. 12, pp. 1626–1633, 2000.
- [28] X. Li, G. Zhang, X. Bai, X. Sun, X. Wang, E. Wang, and H. Dai, “Highly conducting graphene sheets and Langmuir–Blodgett films,” *Nature Nanotechnology*, vol. 3, no. 9, pp. 538–542, 2008.
- [29] X. Li, W. Cai, J. An, S. Kim, J. Nah, D. Yang, R. Piner, A. Velamakanni, I. Jung, E. Tutuc, S. K. Banerjee, L. Colombo, and R. S. Ruoff, “Large-Area Synthesis of High-Quality and Uniform Graphene Films on Copper Foils,” *Science*, vol. 324, no. 5932, pp. 1312–1314, Jun. 2009.
- [30] P. R. Somani, S. P. Somani, and M. Umeno, “Planer nano-graphenes from camphor by CVD,” *Chemical Physics Letters*, vol. 430, no. 1–3, pp. 56–59, Oct. 2006.
- [31] S. J. Chae, F. Güneş, K. K. Kim, E. S. Kim, G. H. Han, S. M. Kim, H.-J. Shin, S.-M. Yoon, J.-Y. Choi, M. H. Park, C. W. Yang, D. Pribat, and Y. H. Lee, “Synthesis of Large-Area Graphene Layers on Poly-Nickel Substrate by Chemical Vapor Deposition: Wrinkle Formation,” *Advanced Materials*, vol. 21, no. 22, pp. 2328–2333, 2009.
- [32] H. Cao, Q. Yu, R. Colby, D. Pandey, C. S. Park, J. Lian, D. Zemlyanov, I. Childres, V. Drachev, E. A. Stach, M. Hussain, H. Li, S. S. Pei, and Y. P. Chen, “Large-scale graphitic thin films synthesized on Ni and transferred to insulators: Structural and electronic properties,” *Journal of Applied Physics*, vol. 107, no. 4, p. 044310, 2010.
- [33] S. Bhaviripudi, X. Jia, M. S. Dresselhaus, and J. Kong, “Role of Kinetic Factors in Chemical Vapor Deposition Synthesis of Uniform Large Area Graphene Using Copper Catalyst,” *Nano Letters*, vol. 10, no. 10, pp. 4128–4133, Oct. 2010.
- [34] K. S. Kim, Y. Zhao, H. Jang, S. Y. Lee, J. M. Kim, K. S. Kim, J.-H. Ahn, P. Kim, J.-Y. Choi, and B. H. Hong, “Large-scale pattern growth of graphene

films for stretchable transparent electrodes,” *Nature*, vol. 457, no. 7230, pp. 706–710, Jan. 2009.

- [35] D. Wei, Y. Liu, Y. Wang, H. Zhang, L. Huang, and G. Yu, “Synthesis of N-Doped Graphene by Chemical Vapor Deposition and Its Electrical Properties,” *Nano Lett.*, vol. 9, no. 5, pp. 1752–1758, May 2009.
- [36] W. A. de Heer, C. Berger, X. Wu, P. N. First, E. H. Conrad, X. Li, T. Li, M. Sprinkle, J. Hass, M. L. Sadowski, M. Potemski, and G. Martinez, “Epitaxial graphene,” *Solid State Communications*, vol. 143, no. 1–2, pp. 92–100, Jul. 2007.
- [37] F. Varchon, R. Feng, J. Hass, X. Li, B. N. Nguyen, C. Naud, P. Mallet, J.-Y. Veuillen, C. Berger, E. H. Conrad, and L. Magaud, “Electronic Structure of Epitaxial Graphene Layers on SiC: Effect of the Substrate,” *Phys. Rev. Lett.*, vol. 99, no. 12, p. 126805, 2007.
- [38] J. Hass, W. A. de Heer, and E. H. Conrad, “The growth and morphology of epitaxial multilayer graphene,” *Journal of Physics: Condensed Matter*, vol. 20, no. 32, p. 323202, Aug. 2008.
- [39] Z. Liu, Q. Liu, Y. Huang, Y. Ma, S. Yin, X. Zhang, W. Sun, and Y. Chen, “Organic Photovoltaic Devices Based on a Novel Acceptor Material: Graphene,” *Advanced Materials*, vol. 20, no. 20, pp. 3924–3930, 2008.
- [40] S. Ghosh, I. Calizo, D. Teweldebrhan, E. P. Pokatilov, D. L. Nika, A. A. Balandin, W. Bao, F. Miao, and C. N. Lau, “Extremely high thermal conductivity of graphene: Prospects for thermal management applications in nanoelectronic circuits,” *Appl. Phys. Lett.*, vol. 92, no. 15, Apr. 2008.
- [41] J. R. Miller, R. A. Outlaw, and B. C. Holloway, “Graphene Double-Layer Capacitor with ac Line-Filtering Performance,” *Science*, vol. 329, no. 5999, pp. 1637–1639, Sep. 2010.
- [42] T. Ramanathan, A. A. Abdala, S. Stankovich, D. A. Dikin, M. Herrera-Alonso, R. D. Piner, D. H. Adamson, H. C. Schniepp, X. Chen, R. S. Ruoff, S. T. Nguyen, I. A. Aksay, R. K. Prud’homme, and L. C. Brinson, “Functionalized graphene sheets for polymer nanocomposites,” *Nat. Nanotechnol.*, vol. 3, no. 6, pp. 327–331, Jun. 2008.
- [43] H. Chen, M. B. Müller, K. J. Gilmore, G. G. Wallace, and D. Li, “Mechanically Strong, Electrically Conductive, and Biocompatible Graphene Paper,” *Advanced Materials*, vol. 20, no. 18, pp. 3557–3561, 2008.
- [44] T. J. Booth, P. Blake, R. R. Nair, D. Jiang, E. W. Hill, U. Bangert, A. Bleloch, M. Gass, K. S. Novoselov, M. I. Katsnelson, and A. K. Geim, “Macroscopic Graphene Membranes and Their Extraordinary Stiffness,” *Nano Lett.*, vol. 8, no. 8, pp. 2442–2446, 2008.
- [45] L. Qiu, X. Zhang, W. Yang, Y. Wang, G. P. Simon, and D. Li, “Controllable corrugation of chemically converted graphene sheets in water and potential application for nanofiltration,” *Chem. Commun.*, vol. 47, no. 20, pp. 5810–5812, May 2011.

- [46] B. Jang and A. Zhamu, "Processing of nanographene platelets (NGPs) and NGP nanocomposites: a review," *Journal of Materials Science*, vol. 43, no. 15, pp. 5092–5101, 2008.
- [47] D. A. Dikin, S. Stankovich, E. J. Zimney, R. D. Piner, G. H. B. Dommett, G. Evmenenko, S. T. Nguyen, and R. S. Ruoff, "Preparation and characterization of graphene oxide paper," *Nature*, vol. 448, no. 7152, pp. 457–460, Jul. 2007.
- [48] A. Buchsteiner, A. Lerf, and J. Pieper, "Water Dynamics in Graphite Oxide Investigated with Neutron Scattering," *The Journal of Physical Chemistry B*, vol. 110, no. 45, pp. 22328–22338, Nov. 2006.
- [49] J. Lu, I. Do, L. T. Drzal, R. M. Worden, and I. Lee, "Nanometal-Decorated Exfoliated Graphite Nanoplatelet Based Glucose Biosensors with High Sensitivity and Fast Response," *ACS Nano*, vol. 2, no. 9, pp. 1825–1832, 2008.
- [50] J. Xiang and L. T. Drzal, "Thermal conductivity of exfoliated graphite nanoplatelet paper," *Carbon*, vol. 49, no. 3, pp. 773–778, Mar. 2011.
- [51] S. Stankovich, D. A. Dikin, G. H. B. Dommett, K. M. Kohlhaas, E. J. Zimney, E. A. Stach, R. D. Piner, S. T. Nguyen, and R. S. Ruoff, "Graphene-based composite materials," *Nature*, vol. 442, no. 7100, pp. 282–6, Jul. 2006.
- [52] L. R. Bunnell, "Method for producing thin graphite flakes with large aspect ratios," U.S. Patent 518691916-Feb-1993.
- [53] B. Jang and A. Zhamu, "Processing of nanographene platelets (NGPs) and NGP nanocomposites: a review," *Journal of Materials Science*, vol. 43, no. 15, pp. 5092–5101, 2008.
- [54] A. B. Bourlinos, V. Georgakilas, R. Zboril, T. A. Steriotis, and A. K. Stubos, "Liquid-Phase Exfoliation of Graphite Towards Solubilized Graphenes," *Small*, vol. 5, no. 16, pp. 1841–1845, Aug. 2009.
- [55] <http://xgsciences.com/products.html>
- [56] Z. Gu, L. Zhang, and C. Li, "Preparation of Highly Conductive Polypyrrole/Graphite Oxide Composites via in situ Polymerization," *J. Macromol. Sci. Part B-Phys.*, vol. 48, no. 6, pp. 1093–1102, 2009.
- [57] P. Steurer, R. Wissert, R. Thomann, and R. Mülhaupt, "Functionalized Graphenes and Thermoplastic Nanocomposites Based upon Expanded Graphite Oxide," *Macromolecular Rapid Communications*, vol. 30, no. 4–5, pp. 316–327, Feb. 2009.
- [58] G. Williams, B. Seger, and P. V. Kamat, "TiO₂ -Graphene Nanocomposites. UV-Assisted Photocatalytic Reduction of Graphene Oxide," *ACS Nano*, vol. 2, no. 7, pp. 1487–1491, Jul. 2008.
- [69] S. Lee, K. Lee, and Z. Zhong, "Wafer Scale Homogeneous Bilayer Graphene Films by Chemical Vapor Deposition," *Nano Letters*, vol. 10, no. 11, pp. 4702–4707, Nov. 2010.

- [60] X. Yang, L. Qiu, C. Cheng, Y. Wu, Z.-F. Ma, and D. Li, "Ordered Gelation of Chemically Converted Graphene for Next - Generation Electroconductive Hydrogel Films," *Angewandte Chemie International Edition*, vol. 50, no. 32, pp. 7325–7328, Jun. 2011.
- [61] C. V. Rao, A. L. M. Reddy, Y. Ishikawa, and P. M. Ajayan, "Synthesis and electrocatalytic oxygen reduction activity of graphene-supported Pt₃Co and Pt₃Cr alloy nanoparticles," *Carbon*, vol. 49, no. 3, pp. 931–936, Mar. 2011.
- [62] J. Lu, L. T. Drzal, R. M. Worden, and I. Lee, "Simple Fabrication of a Highly Sensitive Glucose Biosensor Using Enzymes Immobilized in Exfoliated Graphite Nanoplatelets Nafion Membrane," *Chemistry of Materials*, vol. 19, no. 25, pp. 6240–6246, Dec. 2007.
- [63] A. R. Siamaki, A. E. R. S. Khder, V. Abdelsayed, M. S. El-Shall, and B. F. Gupton, "Microwave-assisted synthesis of palladium nanoparticles supported on graphene: A highly active and recyclable catalyst for carbon–carbon cross-coupling reactions," *Journal of Catalysis*, vol. 279, no. 1, pp. 1–11, Apr. 2011.
- [64] P. V. Kamat, "Graphene-Based Nanoarchitectures. Anchoring Semiconductor and Metal Nanoparticles on a Two-Dimensional Carbon Support," *The Journal of Physical Chemistry Letters*, vol. 1, no. 2, pp. 520–527, Jan. 2010.
- [65] B. K. G. Theng, *Formation and properties of clay-polymer complexes*. Amsterdam ; New York: Elsevier Scientific Pub. Co., 1979.
- [66] A. Rogensues, "Nanotech material-based design of multifunctional membranes," Michigan State University Thesis, In progress.
- [67] J. R. Potts, D. R. Dreyer, C. W. Bielawski, and R. S. Ruoff, "Graphene-based polymer nanocomposites," *Polymer*, vol. 52, no. 1, pp. 5–25, Jan. 2011.
- [68] H. Kim, Y. Miura, and C. W. Macosko, "Graphene/Polyurethane Nanocomposites for Improved Gas Barrier and Electrical Conductivity," *Chemistry of Materials*, vol. 22, no. 11, pp. 3441–3450, Jun. 2010.
- [69] L. M. Veca, M. J. Meziani, W. Wang, X. Wang, F. Lu, P. Zhang, Y. Lin, R. Fee, J. W. Connell, and Y.-P. Sun, "Carbon Nanosheets for Polymeric Nanocomposites with High Thermal Conductivity," *Advanced Materials*, vol. 21, no. 20, pp. 2088–2092, May 2009.
- [70] S. Biswas, H. Fukushima, and L. T. Drzal, "Mechanical and electrical property enhancement in exfoliated graphene nanoplatelet/liquid crystalline polymer nanocomposites," *Composites Part A: Applied Science and Manufacturing*, vol. 42, no. 4, pp. 371–375, Apr. 2011.
- [71] R. D. Priestley, C. J. Ellison, L. J. Broadbelt, and J. M. Torkelson, "Structural Relaxation of Polymer Glasses at Surfaces, Interfaces, and In Between," *Science*, vol. 309, no. 5733, pp. 456–459, Jul. 2005.

- [72] A. Bansal, H. Yang, C. Li, K. Cho, B. C. Benicewicz, S. K. Kumar, and L. S. Schadler, "Quantitative equivalence between polymer nanocomposites and thin polymer films," *Nature Materials*, vol. 4, no. 9, pp. 693–698, 2005.
- [73] S. Ansari, A. Kellarakis, L. Estevez, and E. P. Giannelis, "Oriented Arrays of Graphene in a Polymer Matrix by in situ Reduction of Graphite Oxide Nanosheets," *Small*, vol. 6, no. 2, pp. 205–209, Jan. 2010.
- [74] H. J. Salavagione, M. A. Gómez, and G. Martínez, "Polymeric Modification of Graphene through Esterification of Graphite Oxide and Poly(vinyl alcohol)," *Macromolecules*, vol. 42, no. 17, pp. 6331–6334, Sep. 2009.
- [75] M. Yoonessi and J. R. Gaier, "Highly Conductive Multifunctional Graphene Polycarbonate Nanocomposites," *ACS Nano*, vol. 4, no. 12, pp. 7211–7220, Dec. 2010.
- [76] A. L. Higginbotham, J. R. Lomeda, A. B. Morgan, and J. M. Tour, "Graphite Oxide Flame-Retardant Polymer Nanocomposites," *ACS Appl. Mater. Interfaces*, vol. 1, no. 10, pp. 2256–2261, Oct. 2009.
- [77] D. Chen, H. Zhu, and T. Liu, "In Situ Thermal Preparation of Polyimide Nanocomposite Films Containing Functionalized Graphene Sheets," *ACS Applied Materials & Interfaces*, vol. 2, no. 12, pp. 3702–3708, Dec. 2010.
- [78] J. Liang, Y. Huang, L. Zhang, Y. Wang, Y. Ma, T. Guo, and Y. Chen, "Molecular-Level Dispersion of Graphene into Poly(vinyl alcohol) and Effective Reinforcement of their Nanocomposites," *Adv. Funct. Mater.*, vol. 19, no. 14, pp. 2297–2302, Jul. 2009.
- [79] A. Satti, P. Larpent, and Y. Gun'ko, "Improvement of mechanical properties of graphene oxide/poly(allylamine) composites by chemical crosslinking," *Carbon*, vol. 48, no. 12, pp. 3376–3381, Oct. 2010.
- [80] M. Hirata, T. Gotou, S. Horiuchi, M. Fujiwara, and M. Ohba, "Thin-film particles of graphite oxide 1:: High-yield synthesis and flexibility of the particles," *Carbon*, vol. 42, no. 14, pp. 2929–2937, 2004.
- [81] D. R. Paul and L. M. Robeson, "Polymer nanotechnology: Nanocomposites," *Polymer*, vol. 49, no. 15, pp. 3187–3204, Jul. 2008.
- [82] F. de C. Fim, J. M. Guterres, N. R. S. Basso, and G. B. Galland, "Polyethylene/graphite nanocomposites obtained by in situ polymerization," *Journal of Polymer Science Part A: Polymer Chemistry*, vol. 48, no. 3, pp. 692–698, Feb. 2010.
- [83] J. Y. Jang, M. S. Kim, H. M. Jeong, and C. M. Shin, "Graphite oxide/poly(methyl methacrylate) nanocomposites prepared by a novel method utilizing macroazoinitiator," *Composites Science and Technology*, vol. 69, no. 2, pp. 186–191, Feb. 2009.
- [84] S. H. Lee, D. R. Dreyer, J. An, A. Velamakanni, R. D. Piner, S. Park, Y. Zhu, S. O. Kim, C. W. Bielawski, and R. S. Ruoff, "Polymer Brushes via Controlled, Surface-Initiated Atom Transfer Radical Polymerization (ATRP)

from Graphene Oxide,” *Macromolecular Rapid Communications*, vol. 31, no. 3, pp. 281–288, 2010.

- [85] S. Sun, Y. Cao, J. Feng, and P. Wu, “Click chemistry as a route for the immobilization of well-defined polystyrene onto graphene sheets,” *Journal of Materials Chemistry*, vol. 20, no. 27, p. 5605, 2010.
- [86] L. M. Veca, F. Lu, M. J. Mezzani, L. Cao, P. Zhang, G. Qi, L. Qu, M. Shrestha, and Y.-P. Sun, “Polymer functionalization and solubilization of carbon nanosheets,” *Chemical Communications*, no. 18, p. 2565, 2009.

CHAPTER TWO

Polymer nanocomposites with graphene-based hierarchical fillers as materials for multifunctional water treatment membranes

Abstract

Phase inversion of polymer casting mixtures filled with hierarchical functional nanostructures is proposed as a synthetic route for the design of multifunctional membranes. The study tested the hypothesis that by regulating the relative content of components representing different levels in the nanofiller hierarchy, the structure and additional functions of such membranes could be controlled separately. Exfoliated graphite nanoplatelets (xGnPs) decorated by Au nanoparticles (Au NPs), used as a model hierarchical nanofiller, were added to the casting mixture polysulfone, N- Methyl-2-pyrrolidone and polyethylene glycol prior to forming the membrane by phase inversion. The resulting porous asymmetric nanocomposites were shown to be permselective and catalytically active ultrafiltration membranes that were more resistant to compaction, more permeable than xGnP-free membranes and at least as selective. By designing membrane compositions with different relative amounts of Au-decorated xGnPs and Au-free xGnPs, the structure (controlled by the loading of xGnPs) and catalytic activity (controlled by the loading of Au NPs) could be controlled largely independently.

2.1 Introduction

Recent advances in the synthesis and characterization of engineered nanomaterials have brought about new concepts for the design of membranes with increased permeability, selectivity, and resistance to fouling [1][2].

Nanomaterials such as metal oxide nanoparticles, carbon nanotubes, zeolites, C₆₀ fullerenes, and stacked graphene films can be used to modify and enhance membrane properties [3–11]. The permeability and selectivity of polysulfone-ZrO₂ nanocomposite membranes can be tuned by sintering the ZrO₂ fillers at different temperatures [3]. Membranes based on aligned multiwalled carbon nanotubes support ultrahigh flux and selective separations [4]. Reverse osmosis membranes with a nanocomposite zeolite-polyamide dense layer show significantly improved permeability over commercial polyamide counterparts, while maintaining comparable rejection of NaCl [10]. Membranes modified with nano-Ag, C₆₀ fullerenes and carbon nanotubes show improved resistance to biofouling [5][7][9][11]. The selectivity of GO membranes can be closely regulated by controlling the corrugation of the individual graphene sheets [6], while similar graphene membranes show 10 orders of magnitude higher transport rates of water over helium [8].

The expanding choice of functional nanoparticles (NPs) opens up another opportunity - the bottom-up design of NP-enabled multifunctional membranes

capable of performing tasks additional to that of separation [12][13]. Such multifunctional membranes combine unique NP-based functionalities with the separation function in one hybrid process to cost-effectively enhance overall treatment efficiency and reduce environmental footprint [14–19]. Hybrid systems combining ozonation and ceramic membrane filtration show dramatic reduction in membrane fouling [14][15]. Membranes with immobilized zero-valent iron in combination with Pd or Ni are efficient in the reductive degradation of toxic chlorinated organics [19]. $\text{TiO}_2/\text{Al}_2\text{O}_3$ membranes with highly controlled spatial distribution of pore sizes and show improved photocatalytic activity [18]. Catalytic NPs can be easily immobilized within polyelectrolyte multilayers on the membrane surface enabling highly efficient catalytic reactions [16][17].

There are non-trivial challenges related to the manufacture and application of nanomaterial-enabled membranes. One difficulty is with controlling NP placement and NP dispersion within membrane to minimize NP aggregation in the host matrix [20–22]. Another challenge is the potential NP loss by the membranes; such unintended "shedding" of NPs would likely decrease membrane's lifetime and raise concerns with regard to potential environmental and health risks associated with released nanomaterials. Further, from both fundamental and practical points of view, one needs to better understand how the structure and function of such membranes are coupled and can be controlled separately.

We propose incorporating NP-based functions into the membrane using hierarchical nanofillers where smaller functional NPs are supported by high aspect ratio particles serving as “carrier mats” and “delivery vehicles” for functional NPs. This extends the concept of graphene-supported nanoarchitectures [23–25] to multifunctional membranes and their use as membrane reactors including environmental applications of the flow-through catalysis. In this work, we use exfoliated graphite nanoplatelets (xGnP) decorated by Au NPs as hierarchical nanofillers to prepare novel polymer nanocomposite membranes and demonstrate how this design concept can enable finer control over membrane’s structure, separation properties, and embedded additional functions.

2.2 Approach

xGnPs are chosen to anchor and serve as delivery vehicles for catalytic Au NPs to ensure their controlled placement within the polymer matrix as well as minimal NP aggregation and loss from the membrane. Thus, the nanofiller hierarchy includes 2 levels: 1) xGnPs embedded within the polymer matrix of the nanocomposite membrane, and 2) smaller function-bearing NPs (catalytic Au NPs) anchored on the surface of xGnPs. Only 2 to 12 nm in thickness, xGnPs are pseudo two-dimensional nanoplatelets with the surface area ranging from $\sim 2 \times 2 \mu\text{m}^2$ to $\sim 15 \times 15 \mu\text{m}^2$ [26]. We denote xGnPs particles modified by Au NPs as “Au-xGnP” while nanocomposite membranes with embedded Au-free xGnP and Au-xGnP particles are denoted “ n % xGnP/PSf” and “Au-xGnP/PSf”, respectively, where n is the weight fraction (in percent) of the filler with respect to polysulfone (PSf).

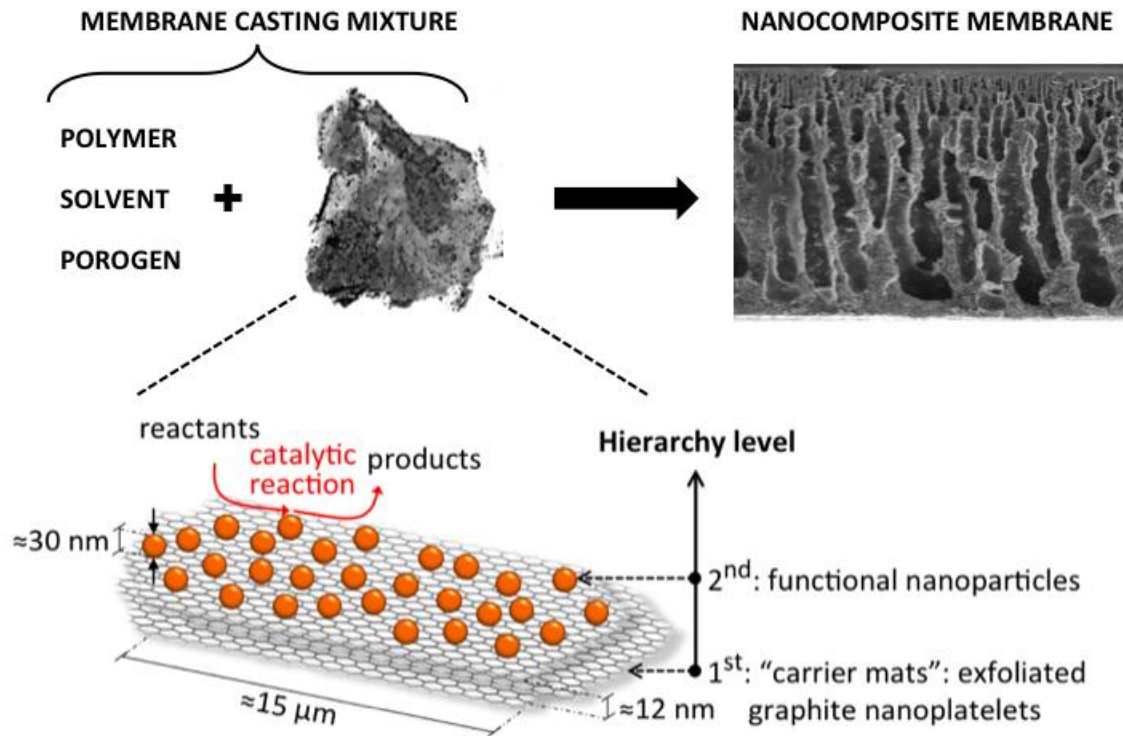


Figure 3: Conceptual illustration of hierarchical nanofillers as building blocks for multifunctional nanocomposite membranes. For interpretation of the references to color in this and all other figures, the reader is referred to the electronic version of this thesis.

We hypothesize that by populating different levels of the nanoparticle hierarchy to different extents, the structure and function of multifunctional membranes can be controlled independently. This can be possible if the structure and function are controlled at different levels of the hierarchy. Such would be the case if, for example, the Au loading controls membrane reactivity and the membrane structure is dependent only on the xGnP loading.

Different levels in the hierarchy were populated by adding decorated xGnPs (Au-xGnP) and non-decorated xGnPs (Au-free xGnP) in different relative amounts to the membrane casting mixture. **Figure 4** illustrates the rationale for the choice of specific compositions. The y-axis gives the total Au loading normalized by the xGnP content of each membrane, while the x-axis gives the xGnP loading as a weight fraction of polysulfone in each membrane. The product of x and y gives the membrane's Au content normalized by the mass of PSf. Relative loadings of Au-free-xGnP and Au-xGnP are chosen such that the set of membranes includes a subset of membranes with different contents of xGnPs but the same content of the Au NP catalyst and a subset of membranes with different contents of Au but the same content of the xGnPs.

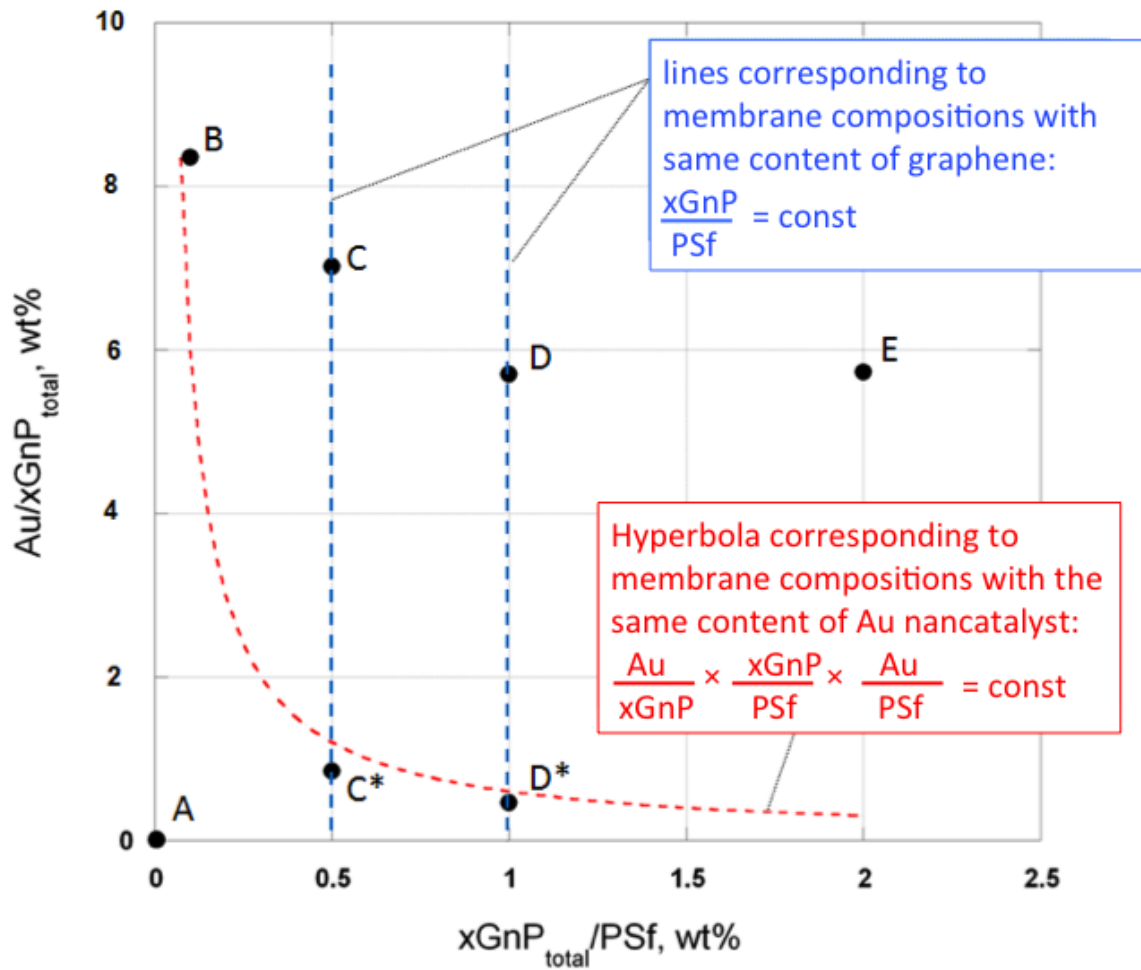


Figure 4: Filler content of nanocomposite membranes (denoted as B, C, C*, D, and D*) evaluated in this study. Filler-free polysulfone membrane (denoted A) is indicated as a reference. $xGnP_{total}$ denotes the mass of embedded xGnP originating from both non-decorated xGnPs and Au-decorated xGnPs. See **Table 1** for the detailed composition of each membrane.

Compositions of the membranes for the former subset are denoted by points that lie along the hyperbola. Specifically, the compositions of 0.1% Au-xGnP/PSf (B), (0.1% Au-xGnP + 0.4% xGnP)/PSf (C*), and (0.1% Au-xGnP + 0.9% Au-xGnP)/PSf (D*) membranes are chosen so that they have the same Au loading of 0.5% Au/PSf. These three compositions lie on the hyperbola where $(\text{Au}/\text{xGnP}) \cdot (\text{xGnP}/\text{PSf}) = 0.5\% \text{ Au}/\text{PSf}$. If the hypothesis stated above is correct, these membranes should exhibit the same catalytic activity yet have different permeability and selectivity. Compositions of the membranes for the latter subset correspond to data points that lie along vertical lines; specifically, nanocomposite membrane pairs C-C* and D-D* have the xGnP loading of 0.5 % xGnP/PSf and 1% xGnP/PSf, respectively. The difference in $\text{Au}/\text{xGnP}_{\text{total}}$ values for membranes B, C, D, and E was due to the batch-to-batch variability on the extent of xGnP coverage by nano-Au (see sections 3.4.3 and 4.1).

The model reaction used in this study to test the hypothesis is the catalytic reduction of 4-nitrophenol to 4-aminophenol where borohydride is the reducing agent and Au NPs are the catalyst. The reactivity of nanocomposite membranes was characterized by filtering the aqueous solution of 4-nitrophenol and sodium borohydride through the membranes and quantifying the extent of 4-nitrophenol reduction.

2.3 Experimental

2.3.1 Reagents

N-Methyl-2-pyrrolidone (NMP), sodium borohydride, 4-nitrophenol (4-NP), PSf (Solvay, Udel P-3500 LCD pellets, MB8, avg. MW 79 kDa), ethylene glycol (EG) (Jade Scientific), polyethylene glycol with the average MW of 400 Da (PEG400), and 20 wt% aqueous solution of poly(diallyldimethylammonium) chloride (PDADMAC) were all used as received. xGnPs with an average platelet diameter of 15 μ were provided by XG Sciences, Lansing, MI. Gold (III) chloride trihydrate (HAuCl_4 , Sigma-Aldrich) was used for as the Au precursor for Au NP formation. Unless otherwise mentioned, all reagents used were purchased from Sigma-Aldrich. The ultrapure water used in all experiments was supplied by a commercial ultrapure water system equipped with a terminal 0.2 μm cartridge microfilter. Dextrans (5, 12, 25, 80, and 150 kDa; DIN certified standard, Sigma-Aldrich) were used as rejection probes.

2.3.2 Preparation and characterization of Au-xGnP nanoparticles

Nanogold-decorated xGnPs (Au-xGnPs) were fabricated via a polyol route [27–30]. The procedure, which was adapted from [30], used HAuCl_4 as the gold precursor, EG as the reducer for the precursor, PDADMAC as the dispersant, and included the following four steps:

- 1) A desired quantity of xGnPs was added to a mixture containing 50 mL of EG and 1 mL of a 20 wt% aqueous solution of PDADMAC and the resulting suspension was sonicated for 12 h to disperse xGnPs.
- 2) Next, 150 μL of 1 M NaOH and 50 μL of 500 mM HAuCl₄ were added to the xGNP suspension. NaOH was used to adjust the pH, which has been shown to control the size and morphology of the resulting Au NPs [31]. PDADMAC, the dispersion agent, was needed to prevent Au NP aggregation. The suspension was mixed and heated to maintain its temperature at $195^{\circ}\text{C} \pm 4^{\circ}\text{C}$ (near the boiling point of EG, 197°C) for 30 min.
- 3) The mixture was then centrifuged for 1 h at 8,000 rpm to separate Au-xGNP from the solution.
- 4) Finally, separated Au-xGNPs were rinsed in acetone to remove residual EG and were allowed to dry overnight in an oven at 100°C . The gold content of prepared Au-xGNP particles was quantified as described in section 2.3.4.3.

2.3.3 Membrane preparation

Membranes were prepared using wet phase inversion. The composition of each casting mixture is given in **Table 1** (also see **Figure 4**). The relative content of PSf (20%wt), NMP (65%wt), and PEG400 (15%wt) was the same for all membranes. The PSf content of 20%wt was chosen as it results in sufficiently viscous, easy-to-cast mixtures and nanocomposite membranes with permeability and rejection values typical for ultrafiltration (20 to $110 \text{ L}/(\text{m}^2 \cdot \text{h} \cdot \text{bar})$) for all but

highest xGnP loading nanocomposite membranes. Also, it was found that at lower polymer contents xGnPs tended to escape the cast film when immersed into the phase inversion bath. The relatively high porogen content (15%) was used to produce membranes with higher permeability.

2.3.3.1 Preparation of polysulfone membranes

PSf membranes were cast using the wet phase inversion procedure. PSf pellets and PEG400 were added to a 50 mL flask containing NMP. The mixture was stirred on a heating plate at 60°C for 24 h or until the PSf pellets were dissolved. After complete homogenization of the mixture, it was cast as a thin film with a drawdown thickness of $300 \pm 1 \mu\text{m}$ on a 20 cm \times 50 cm flat glass plate using a micrometric film applicator (Model 3570, Elcometer). Immediately after casting, the film was immersed in a water bath ($\sim 22^\circ\text{C}$) to initiate phase inversion. The obtained freestanding membrane sheets were thoroughly rinsed with deionized water to remove residual NMP.

Table 1: Composition of membrane casting mixtures for polysulfone membranes (controls) and for nanocomposite membranes with different loadings of xGnP and Au-xGnP.

| Membrane type | | Components of the casting mixture | | | | | Mass loading of xGnP and Au-xGnP (% of the mass of PSf) | | |
|---------------|------------------------------|-----------------------------------|------------|---------------|--------------|--------------|--|---------|----------------|
| | | PSf (g) | NMP (g) | PEG400 (g) | xGnP (mg) | Gold (mg) | xGnP | Au-xGnP | (xGnP+Au-xGnP) |
| A | PSf | 3 | 9.75 | 2.25 | 0 | 0 | 0 | 0 | 0 |
| B | 0.1% Au-xGnP/PSf | | | | 3 | 0.25 | 0 | 0.1 | 0.1 |
| C | 0.5% Au-xGnP/PSf | | | | 15 | 1.1 | 0 | 0.5 | 0.5 |
| C* | Au-xGnP(0.1%)/xGnP(0.4%)/PSf | | | | | 0.13 | 0.4 | 0.1 | |
| D | 1.0% Au-xGnP/PSf | | | | 30 | 1.7 | 0 | 1.0 | 1.0 |
| D* | Au-xGnP(0.1%)/xGnP(0.9%)/PSf | | | | | 0.14 | 0.9 | 0.1 | |
| E | 2.0% Au-xGnP/PSf | | | | 60 | 3.4 | 0 | 2.0 | 2.0 |

2.3.3.2 Preparation of nanocomposite membrane

Three types of nanocomposite membranes were prepared: (i) xGnP/PSf, which were PSf membranes filled with xGnPs, (ii) Au-xGnP/PSf, which were PSf membranes filled with Au-decorated xGnPs, and (iii) xGnP/Au-xGnP/PSf, which were PSf membranes filled with a mixture of gold-free xGnPs and Au-decorated xGnPs. To prepare these membranes, the standard wet phase inversion technique described in section 2.2.1 was slightly modified. First, a desired quantity of Au-xGnP or Au-free xGnP or a mixture of the two was suspended in NMP and was sonicated (bath sonicator Aquasonic 50T, VWR Scientific) for 1 h to produce xGnP/NMP organosol. Second, PSf pellets and PEG400 were added to the xGnP/NMP organosol, and the mixture was stirred at 60 °C for 24 h allowing the PSf to dissolve. The membrane was cast, rinsed, and stored in the same manner as the PSf membrane.

The xGnP loading in the resulting casting mixture was calculated as mass percent of xGnP with respect to PSf. In preparing nanocomposite membranes filled with Au-xGnPs, the casting mixtures had xGnP loadings of 0.1%, 0.5%, 1.0%, and 2.0%. In preparing nanocomposite membranes filled with a mixture of xGnPs and Au-xGnPs, the casting mixture had xGnP loadings of 0.5% (0.1% of Au-xGnP + 0.4% of xGnP) and 1% (0.1% of Au-xGnP + 0.9% of xGnP).

2.3.4 Membrane characterization

Each cast membrane was characterized for permeability, molecular weight cutoff (MWCO), mechanical properties, catalyst content, and catalytic activity. The permeability, MWCO, and catalytic activity were determined in the following sequence of steps:

- 1) 4-NP solution was filtered at a pressure of 20 psi. During this period of filtration, membranes were compacted and the 4-NP adsorption capacity of the membrane was exhausted;
- 2) Membrane permeability was measured;
- 3) 4-NP and borohydride solution was filtered at four different pressures in steps from highest to lowest pressure (20, 16, 12, and 8 psi) to quantify catalytic activity;
- 4) The membrane was rinsed with DI water;
- 5) The membrane was challenged with 500 mg/L dextran solutions of various molecular weights to measure the MWCO.

In addition scanning electron microscopy (SEM) and transmission electron microscopy (TEM) were used to characterize morphology of membranes.

2.3.4.1 Membrane permeability and molecular weight cutoff

Permeate flux was measured by recording the mass of the permeate collected on a balance interfaced with a computer. After compaction at the transmembrane pressure of 1.38 bar (20psi) and solution temperature of 22 ± 2 °C, membrane

permeability was measured as the steady state value of the permeate flux normalized by the transmembrane pressure.

To determine the MWCO of the membranes, they were challenged by a set of aqueous solutions of dextrans of five different molecular weights (5, 12, 25, 80, and 150 kDa, Sigma Aldrich). A stirred ultrafiltration cell (model 8010, Millipore) was used in all rejection experiments. For each cast membrane, three coupons were tested. Between experiments with dextrans of different molecular weights, the membrane coupon was thoroughly rinsed by filtering 10 mL of DI water through it. The efficiency of rinsing cycle was validated by measuring residual dextran concentration of both the feed and permeate. Total organic carbon analyzer (OI Analytical model 1010 Analyzer, College Station, TX) was used to determine dextran concentrations.

2.3.4.2 Mechanical properties

Tensile strength, modulus of elasticity, and percentage of elongation were measured using a tensile testing unit (SFM-20, United Testing Systems, Inc. CA) at room temperature. Five specimens from each membrane were tested. The specimens were of the Type IV dog bone shape and were cut using a die and hydraulic press. The measurements were performed according to ASTM D638-10 method (2006) with an extension rate of 1.27 mm/min.

2.3.4.3 Catalyst content of nanocomposite membranes

To quantify the mass of gold immobilized on xGnP surface in the form of NPs, gold was stripped off xGnPs by leaching and the concentration of gold was measured in the leachate. The procedure included four steps:

1. A weighed amount of Au-xGnP powder (or a weighed sample of a cast Au-xGnP/PSf membrane) was heated in aqua regia at its boiling point (109 °C) for 1 h.
2. Immediately after heating, the suspension was placed in a water bath (22⁰C) and sonicated (bath sonicator Aquasonic 50T, VWR Scientific) for 3 h.
3. The sonicated suspension was filtered through a 0.45 µm mixed cellulose ester filter (Millipore, Billerica, MA).
4. The filtrate was diluted with DI water and analyzed for gold content using atomic adsorption microscopy (Perkin-Elmer 1100, Waltham, MA.) Because not all gold was leached from Au-xGnP, the cake on the surface of the 0.45 µm filter was analyzed for gold content. To do that the filter was dried in a fume hood for 12 h and the dried membrane coated with a layer of xGnP was weighed, suspended in fresh aqua regia and subjected to the sequence of treatment steps 2 to 4 three times. At the end, the gold concentration in the filtrate was less than 4% of the total leached gold concentration.

2.3.4.4 Catalytic activity

In characterizing the reactivity of the membranes, aqueous solution of 4-NP was used as the feed. The catalytic reduction of 4-NP to 4-aminophenol (4-AP) by sodium borohydride (NaBH_4) in the presence gold NPs (the catalyst) is a well-known reaction that is often used as a benchmark reaction for testing catalytic activity of NPs (e.g., [32][33]) .

To ensure that the observed reduction of 4-NP was due to the catalytic reaction and not due to adsorption, up to 800 mL of 0.6 mM aqueous solution of 4-NP was filtered through the membrane prior to the catalytic reduction experiment. These “exhaustion” experiments were carried out using a stirred ultrafiltration cell (model 8050, Millipore) connected to a 5 L stainless steel feed tank (Alloy Products, Co.) pressurized at 20 psi (and 40 psi where mentioned; see Supporting Information (SI)). The feed solution was contained in a glass flask placed in the pressure vessel; this arrangement was necessary to minimize degradation of the 4-NP caused by the contact of the feed solution with the steel walls of the feed tank. The filtration was carried out for 120 min or until the permeate concentration of 4-NP was less than 4% of the feed concentration. 4-NP concentrations were measured using UV-Vis spectrophotometry at 400 nm.

4-NP feed solutions used in catalytic reduction experiments were prepared in the same manner as solutions used during compaction and exhaustion stages, except that 4-NP was dissolved in a 50 mM aqueous solution of NaBH_4 and not the DI water. The concentration of NaBH_4 was assumed constant throughout the

reaction. The concentration of 4-NP in the feed solution was measured between each pressure step to observe any 4-NP degradation that could occur during the filtration experiment. The average and maximum degradation of 4-NP feed solution were $1.3 \pm 0.44\%$ and 5.8%, respectively. The initial concentration of 4-NP in the glass flask contained in the pressure vessel was used as the feed concentration to determine the 4-NP reduction in permeate samples. The same filtration apparatus, which was used to compact the membrane and exhaust its adsorptive capacity with respect to 4-NP, was used in catalytic reaction experiments.

After the membrane was fully compacted and its adsorptive capacity was exhausted, a 0.6 mM 4-NP solution in 50mM NaBH₄ was filtered through the membrane in a test where the transmembrane pressure was decreased step-wise from 20 psi to 16 psi, to 12 psi, to 8 psi. Filtration at each transmembrane pressure lasted for approximately 40 min at lower permeate fluxes and 15 min at higher permeate fluxes. Lower transmembrane pressures lead to lower permeate fluxes, higher residence times for 4-NP in the membrane and, therefore, lower fractions of 4-NP reduced to 4-AP. Based on the values of permeate flux and 4-NP concentrations in the feed and the permeate, the reaction flux was calculated (see section 4.6) and used as a quantitative measure of the catalytic activity of membranes.

2.3.4.5 SEM and TEM imaging

SEM images of prepared membranes were recorded using a JOEL 6400 and a JOEL 7500 microscopes. Membrane cross sections were prepared by freeze fracturing small (approximately 2cm × 2cm) membrane specimens in liquid nitrogen. The specimens were mounted on aluminum stubs using carbon paint and imaged at an accelerating voltage of 10 kV.

TEM images of Au-xGnPs and xGnP particles were recorded using a JEOL 100 CX TEM. A 10 µL droplet of xGnP particles suspended in acetone was dropped onto 300 mesh standard copper grids. The TEM was operated at an accelerating voltage of 100 kV, with a maximum theoretical resolution of 0.2 nm. Micrographs were recorded using a MegaView III Camera (Soft Imaging System, Lakewood, CO). TEM images of nanocomposite cross-sections were analyzed using the public domain NIH ImageJ program, version 1.43u (developed at the U.S. National Institutes of Health and available on the Internet at <http://rsb.info.nih.gov/ij>).

2.4 Results and discussion

2.4.1 Properties of Au-xGnP nanoparticles

The polyol method [27] and its modified versions [30][34][35] have been used extensively for decorating graphene with noble and base metal NPs such as cobalt, nickel, and copper. The method involves the reduction of a metal-salt

precursor to metal ions in a polyol solution, wherein ions nucleate to form metal NPs. The mechanism that supports the nucleation of metal ions on a carbon surface has been described as both preferential adsorption [35] and formation of electron-donor complexes [36]. Preferential adsorption takes place when high surface energy metal nuclei form in solution and then adsorb to the carbon support. Electron donor-acceptor complexes form between the metal ions and the basal plane of the carbon support that has π -electron rich regions [37][38] which support the nucleation of metal ions at the carbon surface through a donor-acceptor interaction [36]. The clustering of Au NPs along the perimeter of xGnPs is most likely due to the interactions of Au with surface oxides mainly located along the edges of the nanoplatelets.

Figure 5 presents SEM (A, B) and TEM (C, D) images of xGnP decorated with Au NPs. While most Au NPs had diameters in the 10 nm to 50 nm range, a small fraction (less than 10%) of Au NPs observed on the xGnP support were as large as 100 nm. The gold content of Au-xGnPs, as determined by atomic adsorption analysis, showed batch-to-batch variation from 5.0% to 8.4% by mass of Au with respect to xGnP. We attribute the observed variability in Au NP size, the degree of xGnP coverage by Au NPs and homogeneity of their distribution over xGnP surface to the sensitivity of Au NP formation to experimental conditions such as mixing rate and oil bath temperature. To minimize Au NP aggregation and, thereby, improve reproducibility of xGnP coverage by Au NPs fresh solutions of NaOH were prepared for each decoration experiment.

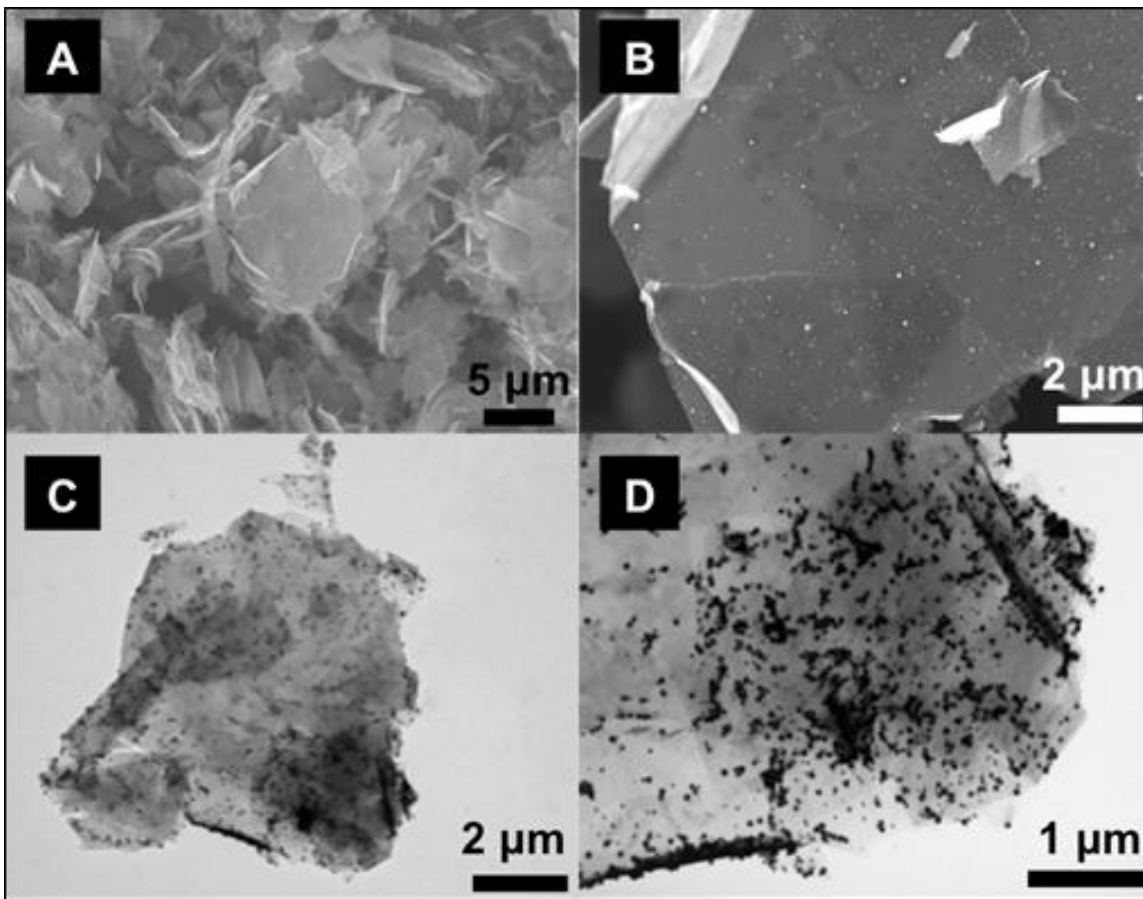


Figure 5: SEM (A, B) and TEM (C, D) micrographs of xGnPs (A) and xGnPs decorated by gold nanoparticles (C, D). Figure D is a magnified view of a portion of the platelet shown in Fig. C.

2.4.2 Morphology of nanocomposite membranes

The only difference in the visual appearance of the membranes with different xGnP loadings was their color; nanocomposite membranes were gray with darker shades of gray corresponding to higher xGnP loadings (**Figure 6**).

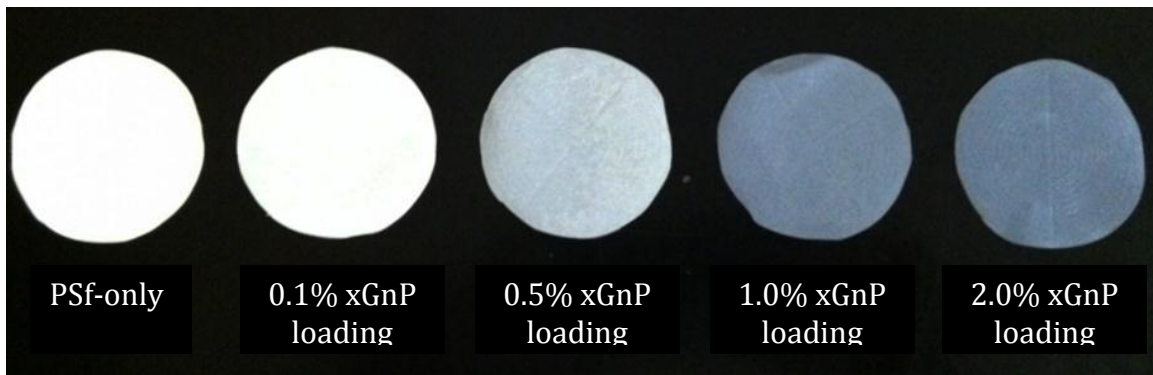


Figure 6: Photographs of membranes with different xGnP loading.

SEM imaging demonstrated that all nanocomposite membranes had an asymmetric porous structure (**Figure 7**) that was a function of the xGnP loading. In the case of xGnP-free membranes, finger-like macrovoids spanned most of the membrane, and more circular macrovoids formed at the permeate side of the membrane. In the case of nanocomposites, the size of circular macrovoids increased with an increase in the xGnP loading (**Figure 7**).

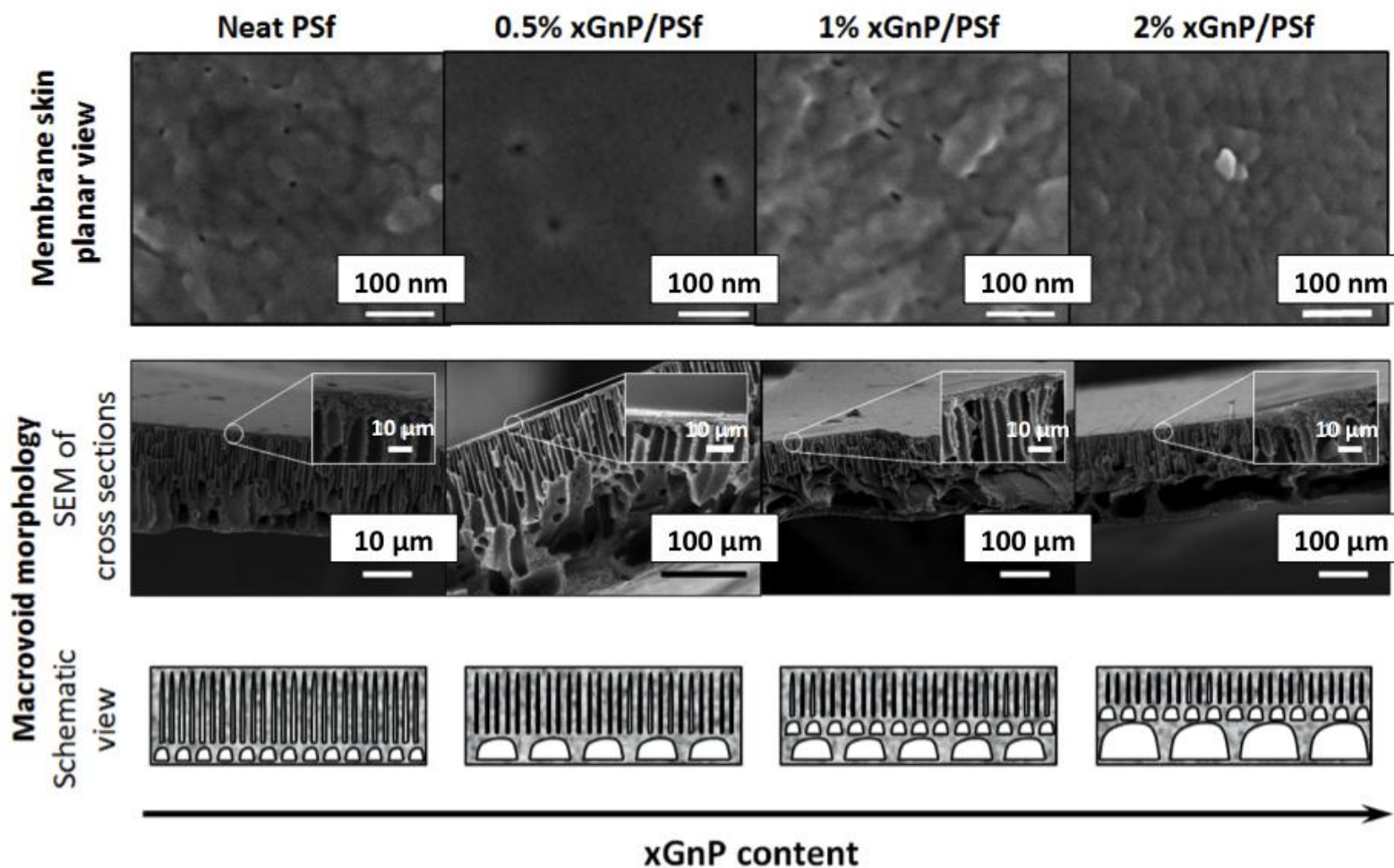


Figure 7: SEM micrographs of membrane skin (top row) and membrane cross-sections (middle row) for a) neat PSf, b) 0.1% xGnP/PSf, c) 1.0% xGnP/PSf, and d) 2.0% xGnP/PSf membranes. The trends in macrovoid morphology as a function of xGnP loading are schematically illustrated in the bottom row.

While xGnPs were located throughout the entire membrane cross-section including the denser layer (**Figure 8**), no xGnPs were found to protrude through the membrane skin and no consistent xGnP-induced changes in the skin morphology were observed.

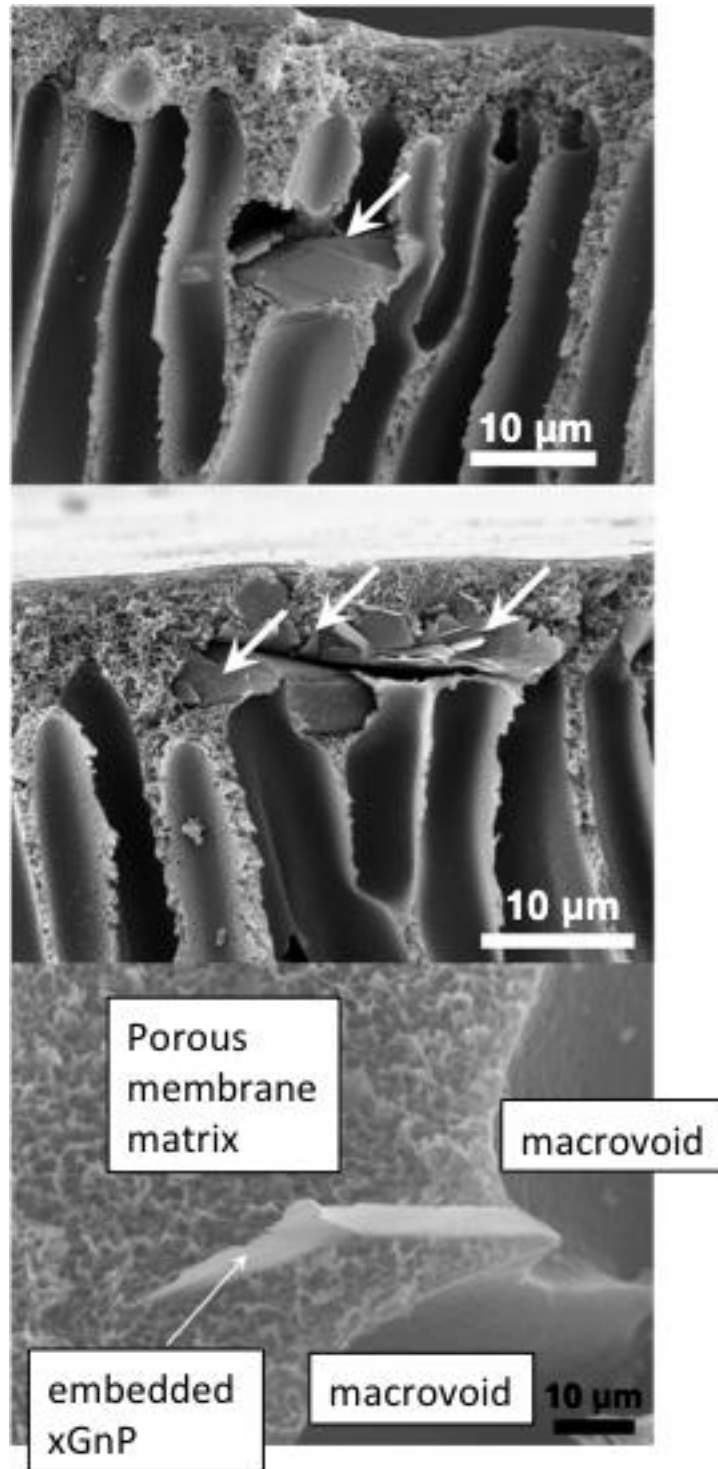


Figure 8: SEM micrographs of xGnPs embedded within the dense top-layer (top, middle) and macrovoid (bottom) regions of xGnP/PSf and Au-xGnP/PSf membranes.

The change in macrovoid size can be interpreted to result from the decrease in the net affinity of the casting mixture to the non-solvent upon the addition of xGnPs. xGnPs have a very large specific surface area; most of the xGnP surface is a relatively hydrophobic basal plane with the water contact angle of 127° [39]. The lower affinity should translate into an earlier onset of demixing, higher propagation rate of the demixing front and, ultimately, a more porous membrane. These trends have been experimentally demonstrated in a recent study when C_{60} NPs were added to a casting mixture of PSf, NMP, and polyvinylpyrrolidone [21].

2.4.3 Permeability and selectivity of nanocomposite membranes

Introduction of only 0.1%wt of xGnPs into the casting mixture resulted in a 22-fold increase in membrane permeability when compared with that of neat PSf membranes (**Figure 9**). Importantly, this increase was accompanied by a statistically significant improvement of selectivity as indicated by an increase in the rejection of 12 kDa dextran from $28\% \pm 5\%$ to $69\% \pm 10\%$. As xGnP loading increased further to 1%wt, the permeability remained relatively constant. The 12 kDa dextran rejection was also maintained at an approximately same level over the (0.1 to 1.0)% range of xGnP loadings but then decreased to the level typical for filler-free PSf membranes when the loading reached 2%wt xGnP/PSf. The MWCO of filler-free PSf membranes and 0.1, 0.5, 1.0, and 2.0%wt xGnP/PSf membranes was 136 ± 29.8 kDa, 36.3 ± 10.5 kDa, 38.8 ± 10.8 kDa, 50.9 ± 10.3

kDa, 135 ± 18.2 kDa, respectively. The simultaneous improvements in permeability and selectivity can be interpreted as resulting from a combination of increased porosity and a decrease in the effective pore size of the membrane skin.

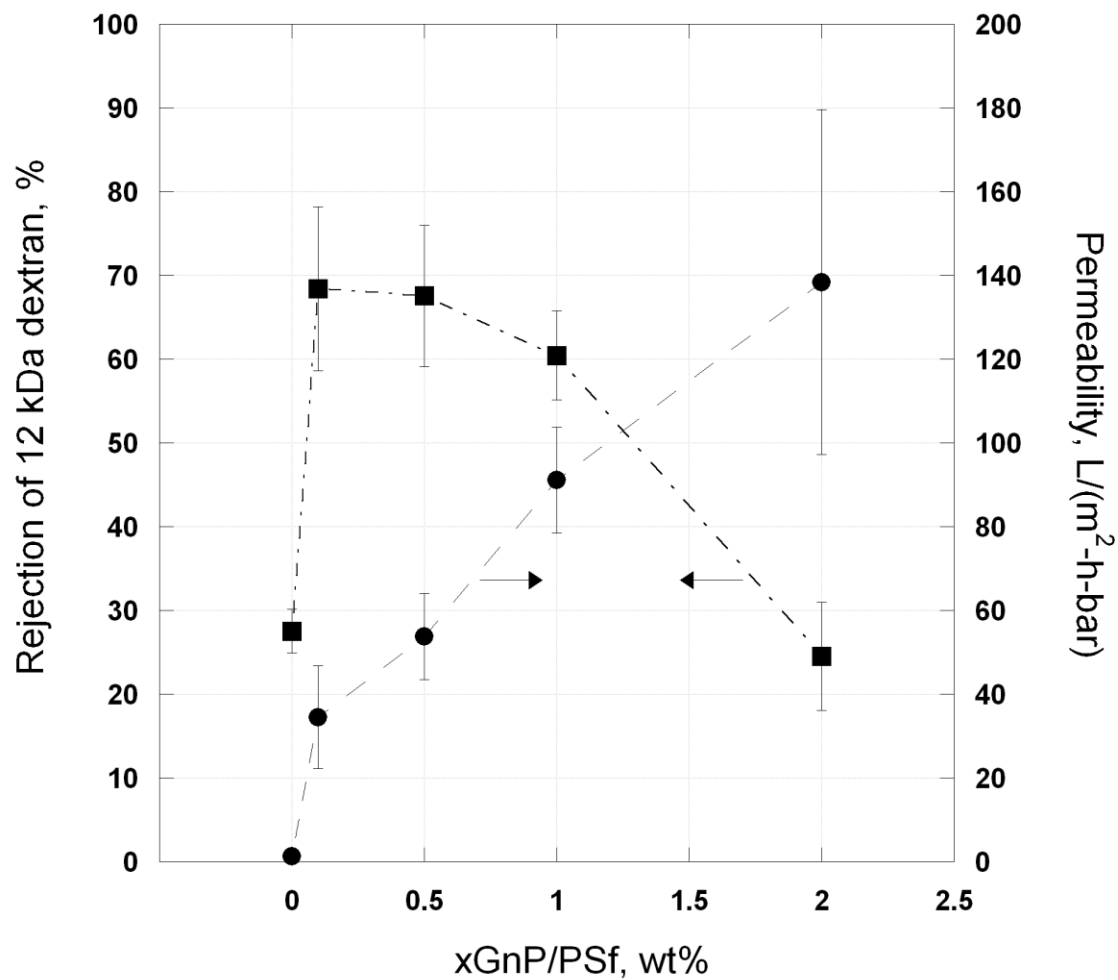


Figure 9: Rejection of 12 kDa dextran and pure water permeability of xGnP/PSf and Au-xGnP/PSf membranes as functions of xGnP loading. The permeability of xGnP-free PSf membranes is 1.3 ± 1.1 L/(m²·h·bar). Error bars correspond to 90% confidence level.

2.4.4 Mechanical properties of nanocomposite membranes

Tensile strength, percent elongation, and modulus of elasticity of membranes decreased with an increase in xGnP loading (**Figure 10**). These decreases can be partly attributed to the larger size of macrovoids, which led to higher bulk porosity of the cast membranes [40] and partly to the low affinity between xGnPs and PSf. Improving the xGnP-polymer affinity should increase the tensile strength of the nanocomposite membranes [41]. We note that mechanical properties of select nonporous nanocomposites (e.g. xGnP-phenylethynyl-terminated polyimide, xGnP-polypropylene) were shown to improve with the addition of xGnPs [26][42].

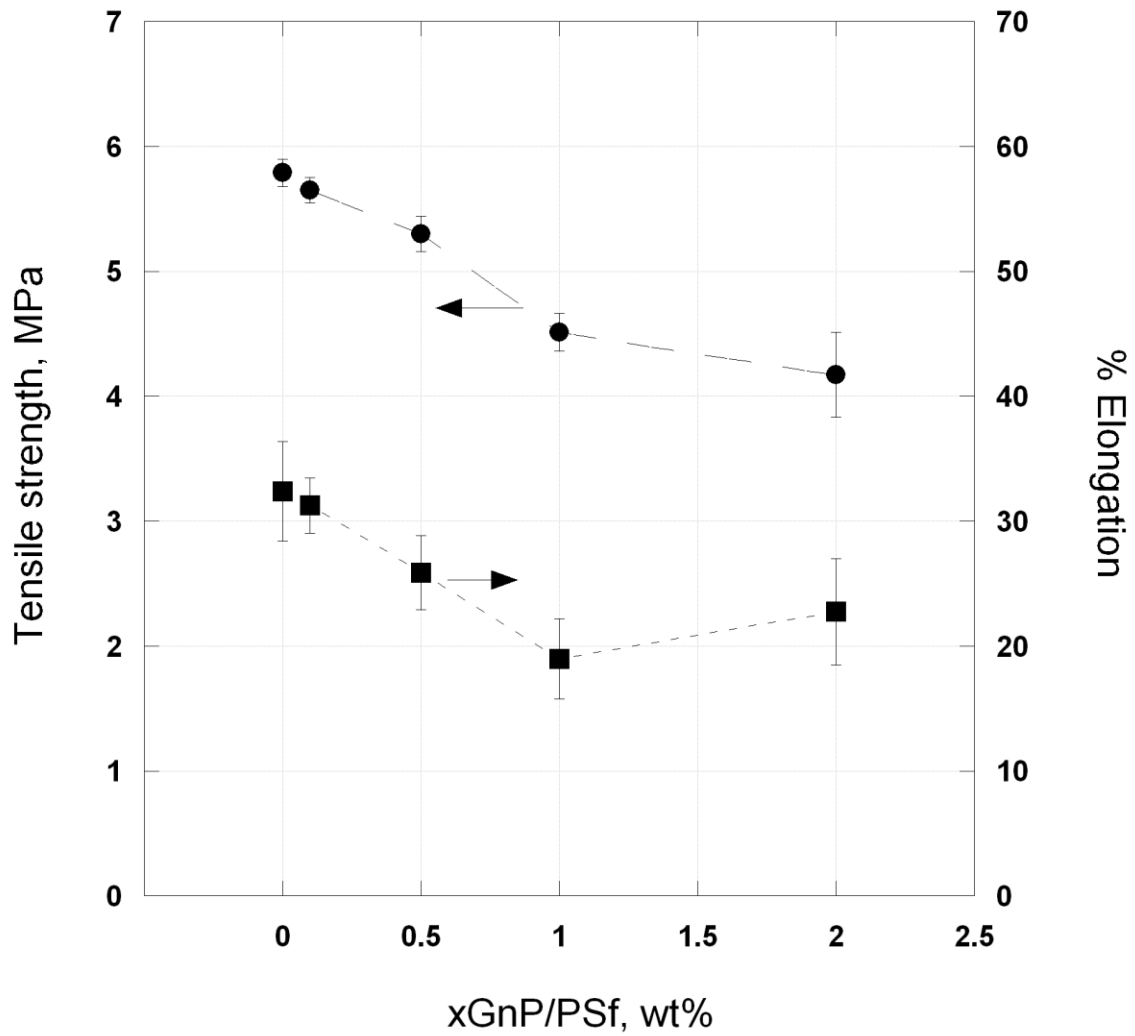


Figure 10: Tensile strength and % elongation of membrane specimens as functions of xGnP loading. Error bars correspond to 90% confidence interval.

2.4.5 Transient behavior of membrane permeability: Apparent compaction resistance of xGnP/PSf membranes

There is abundant evidence in literature that compaction affects performance of both porous and non-porous membranes and that certain composite formulations are more resistant to compaction than their neat polymer homologues [40][43][44]. High transmembrane pressure differentials lead to irreversible changes in the macrovoid structure of the membrane, resulting in decreased pore volumes and non-recoverable losses in hydraulic permeability. In asymmetric membranes, membrane compaction preferentially occurs in the macrovoid structure, and larger macrovoids should cause membranes to be more compactable [43].

The compaction behavior of xGnP-PSF composite membranes changed significantly as a function of xGnP loading (**Figure 11**). In the case of xGnP-free membranes, the permeability declined by the factor 12.7 ± 2.0 as a result of membrane compaction. In contrast, membrane with xGnP/PSf loadings of 0.1%, 0.5%, 1%, and 2% had compaction ratios of 4.1 ± 0.7 , 1.6 ± 0.2 , 1.4 ± 0.1 , and 1.5 ± 0.2 , respectively. Not only was the permeability of xGnP-filled membranes was higher initially (e. g., 91.1 ± 12.6 L/(m²·h·bar) for 1% xGnP/PSf vs 1.3 ± 1.1 L/(m²·h·bar) for xGnP-free PSf membranes) but it could also be sustained at near this higher value. Additionally, as is evident from the comparison of 90% confidence intervals of initial permeability values, nanocomposites showed

significantly less coupon-to-coupon variability in permeability than xGnP-free controls.

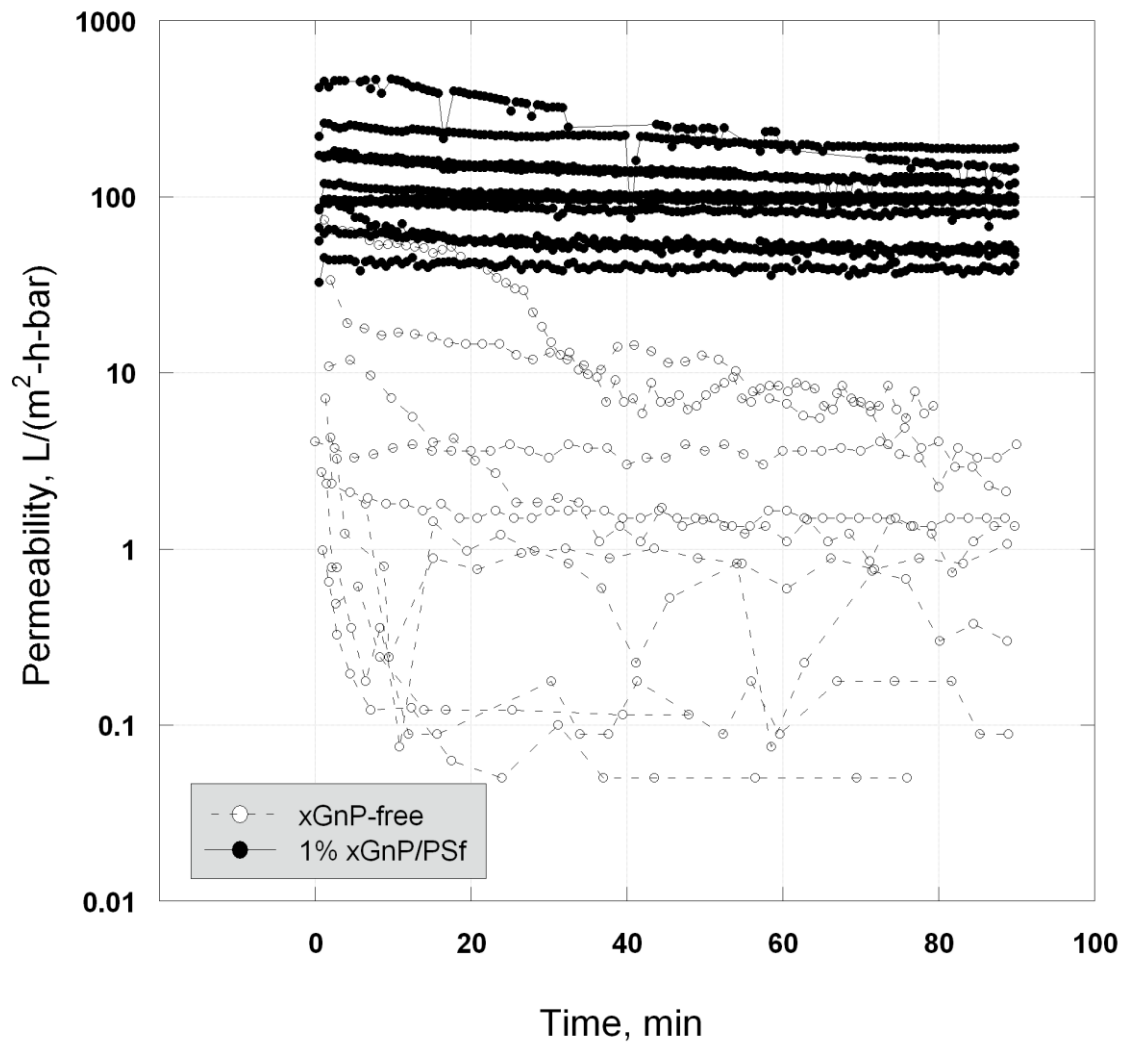


Figure 11: Compaction behavior of neat PSf membranes (-○-) and PSf nanocomposite membranes filled with 1 wt% of xGnP or Au-xGnP (-●-) under the applied transmembrane pressure of 20 psi (1.38 bar).

This apparent reinforcement effect of xGnPs is somewhat surprising given the low affinity between the filler and the host matrix and the statistically significant decrease in the tensile strength and % elongation of the membranes at 1% loading of xGnPs (see section 4.5). It is possible that smaller initial flux declines observed for xGnP-filled membranes are due not to improved compaction resistance but to the formation of preferential flow paths along the boundary between the PSf matrix and embedded xGnPs. If the applied pressure induces movement of xGnPs relatively to the surrounding PSf matrix, high free volume interfacial regions between the polymer and xGnP particle can be created; in this case, increased flow rate along these regions could compensate for the flow rate decrease due to the pressure-induced collapse of PSf pores. Mechanical testing of the compression strength of the membranes could corroborate or disprove that xGnPs reinforce the PSf matrix. Such measurements, however, may not be possible for samples as thin as typical ultrafiltration polymeric membranes.

2.4.6 Catalytic activity of nanocomposite membranes

The catalytic activity of the membranes was quantified in experiments on the catalytic reduction of 4-NP during the filtration of the aqueous solution of 4-NP and NaBH₄. Reduction of nitrophenolates to their corresponding aminophenolates in the presence of NaBH₄ is often used as convenient reaction for characterizing the catalytic activity of noble metal NPs. 4-AP is the only product of this reaction and both 4-NP and 4-AP are easily quantified using UV-

Vis spectroscopy (e.g., [17][45]). In addition, the extent of the reaction could be monitored visually as the reduction of 4-NP is accompanied by a change of the solution color from bright yellow to light yellow to near colorless.

The nanocomposite membranes behaved like plug-flow reactors with the pseudo-first-order decay reaction. The data on 4-NP reduction conformed well to a simple first-order kinetic model:

$$C_l = C_0 \exp \left[-\frac{k_{obs}}{v} \cdot l_{eff} \right], \quad (1)$$

where, C_l is the concentration of 4-NP in the permeate, C_0 is the concentration of 4-NP in the feed, v is the permeate flux (i.e., approach velocity), k_{obs} is the observed first-order reaction rate constant for the membrane, and l_{eff} is the effective length of the membrane. It was assumed that the reaction was at steady state and that dispersion could be neglected. By plotting $\ln(C_l \cdot C_0^{-1})$ against v^{-1} and fitting the dependence with a linear regression, values of $k_{obs} \cdot l_{eff}$ were determined (**Figure 12**).

Because of the complexity of the pore space morphology (unknown distribution of pore sizes as a function of location within the membrane), a lack of information on the fraction of the Au NP surface area unavailable for reaction due to the possible occlusion by the polymer, and the uncertainty with how the catalytic properties of xGnP-immobilized Au NPs compare with those of Au NPs in

suspension, it was impossible to determine values of k_{obs} and l_{eff} separately. Therefore, we used $k_{obs} \cdot l_{eff}$ as an aggregate characteristic of the catalytic activity of the membrane. Because this characteristic describes the extent of the catalytic reaction in the membrane reactor and has units of $m \cdot s^{-1}$ we describe $k_{obs} \cdot l_{eff}$ as “reaction flux.” Per eq. (1), the ratio of reaction flux to the permeate flux determines the extent of the first-order reaction.

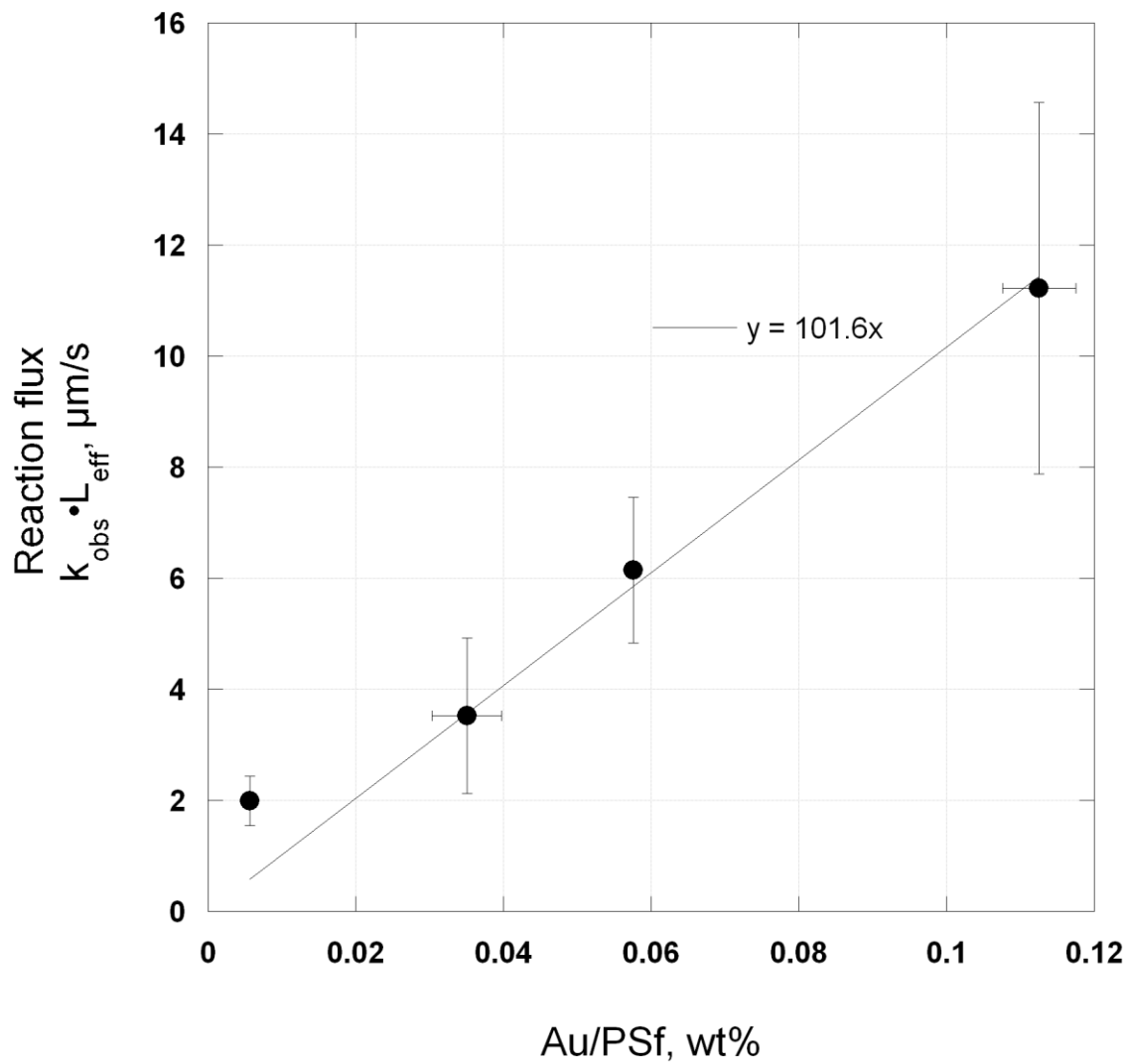


Figure 12: Observed reaction rate constant as a function of Au/PSf loading. Error bars correspond to the 90% confidence interval.

Based on the good fit of the 4-NP reduction data to the first order reaction model we surmise that the reaction takes place mostly within the dense layer with the relatively narrow pore size distribution. This is a likely scenario given that, in the comparison with the macrovoid region, the dense layer has smaller pores facilitating the diffusion of reactants from the bulk of the pore volume to catalyst at the pore surface. This suggests that targeted placement of the catalyst within the dense layer could help increase reaction throughput per unit catalyst mass. Given the increased scatter in reaction flux observed at higher xGnP loadings (Fig. 10), the strategy of targeted placement of the filler may also improve the reproducibility of the catalytic performance.

2.4.7 Independent control of membrane's structure and additional functions

The dependence of reaction flux, $k_{obs} \cdot l_{eff}$, on Au loading could be fit reasonably well with the linear regression (**Figure 13**). The data shown in **Figure 12** represent results of 48 catalytic reduction experiments. Each data point describes reaction flux averaged over multiple membranes with approximately the same content of Au NPs but very different contents of xGnPs. Thus, the scaling indicates that the catalytic activity of the membrane is largely controlled by the loading of catalytic Au NPs (i.e. population of the level 2 of the nanofiller hierarchy) and is relatively independent of the loading of xGnPs (i.e. population of the level 1 of the nanofiller hierarchy.)

By the same token, the permeability showed a statistically significant trend of increasing with an increase in xGnP content although each permeability data point in Fig. 7 represents a value averaged over multiple membranes with very different contents of Au NPs. This indicates that the structure of the membrane is largely controlled by the loading of xGNPs (i.e. population of the level 1 of the nanofiller hierarchy) and is relatively independent of the loading of catalytic Au NPs (i.e. population of the level 2 of the nanofiller hierarchy). This result is rather intuitive: because the larger dimension of xGNPs (15 μm) exceeds the typical pore size in the dense layer of ultrafiltration membranes, one nanoplatelet spans multiple pores within the layer (**Figure 8**, bottom) and can affect membrane structural and separation properties much more than smaller nanoparticles immobilized on the xGnP surface can.

These observations lead to the conclusion that the structure and reactivity of membranes with hierarchical fillers could be controlled relatively independently by regulating the relative content of hierarchy levels in the nanofiller.

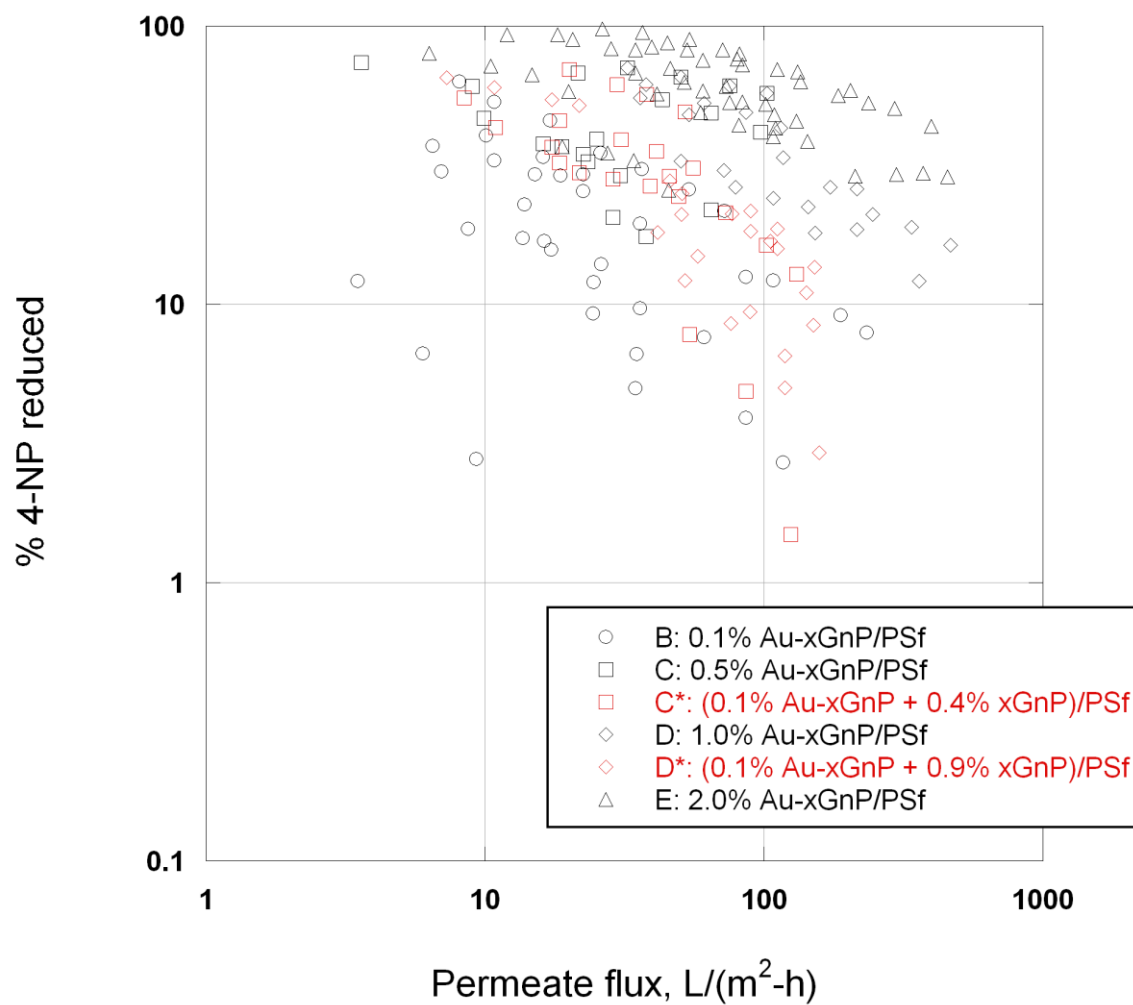


Figure 13: Reduction of 4-nitrophenol as a function of permeate flux for membranes with different Au-xGnP/PSf and (Au-xGnP + xGnP)/PSf loadings.

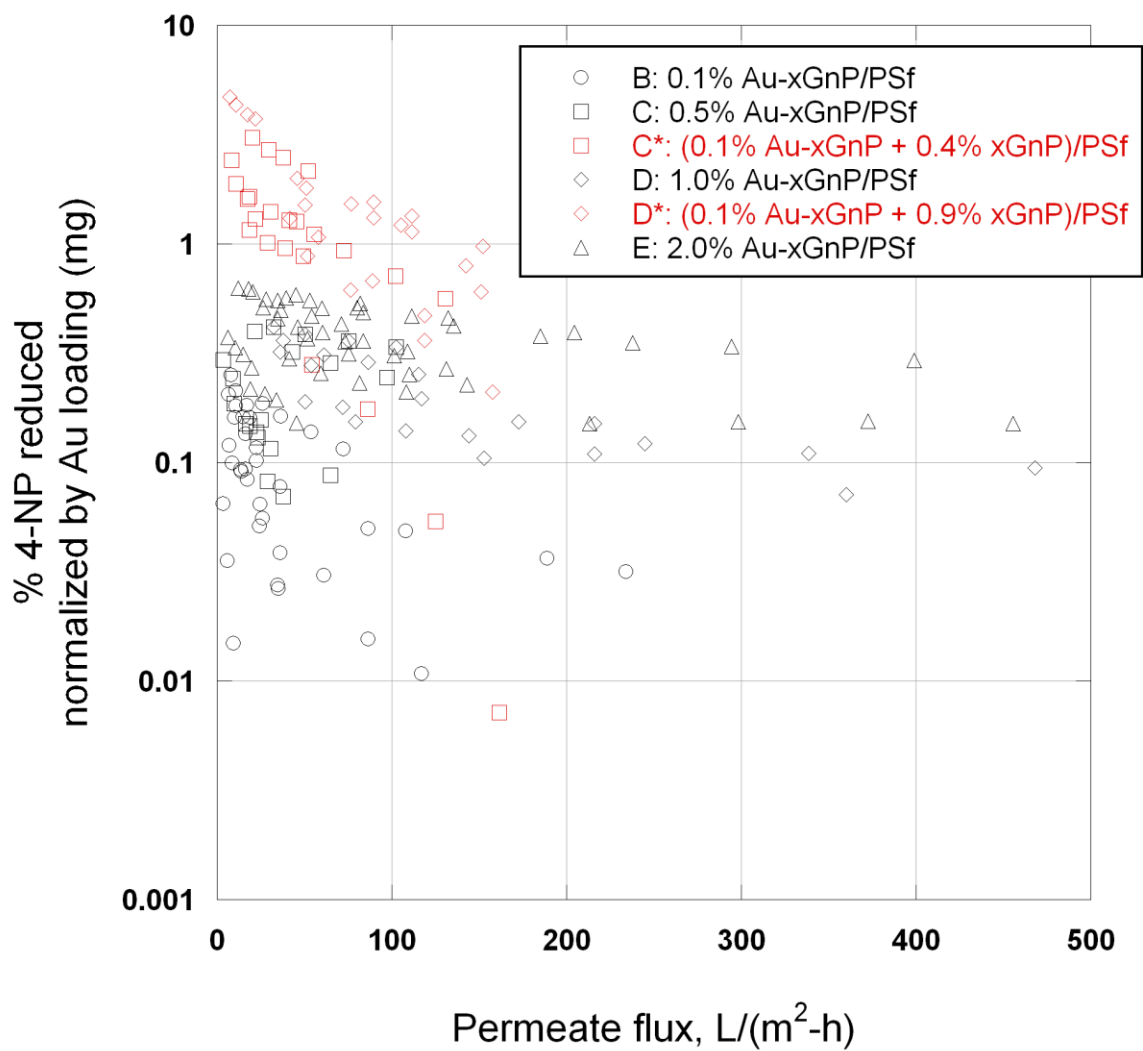


Figure 14: Reduction of 4-nitrophenol normalized by Au content in mg as a function of permeate flux for membranes with different Au-xGnP/PSf and (Au-xGnP + xGnP)/PSf loadings.

A closer look at the data on the extent of 4-NP reduction by nanocomposite membranes of different composition reveals that some degree of coupling between structure and function does exist. **Figure 14** shows that, for the same permeate flux (i.e. approximately the same residence time within the membrane), the catalytic activity of more porous membranes was higher than that of their less porous counterparts with the same catalyst loading (i.e., C* vs C and D* vs D). It appears that the addition of Au-free xGnPs to the membrane not only renders the membrane more permeable but also reduces the occlusion of the immobilized nanocatalyst by the surrounding polymer matrix.

2.4.8 Analysis of statistical significance on the independent control of membrane structure and additional functions

Linear regressions were used to determine the levels of confidence that the reactive flux and permeability are dependent on the two independent variables xGnP/PSf and Au/PSf loadings. Two types of linear regressions are shown in

Table 2. The first two regressions (A) and (B) were computed using two independent variables ($x_{\text{GnP/PSf}}$ and $A_{\text{u/PSf}}$) to determine the extent that the reactive flux and permeability depend on both variables. The next two regressions (C) and (D) were computed using only one independent variable for each regression.

Table 2: Confidence-levels of the reactive flux ($k_{obs} \cdot \ell_{eff}$) and permeability dependence on either both xGnP/PSf and Au/PSf loadings (A and B), or only Au/PSf (C) or xGnP/PSf (D) loadings.

| Linear regression of two dependent variables | | | |
|---|----------------|---------------|-------------------|
| | p-value | t-stat | Confidence |
| (A) $k_{obs} \cdot \ell_{eff}$ depends on xGnP/PSf | 0.4299 | 0.797 | 57.0% |
| $k_{obs} \cdot \ell_{eff}$ depends on Au/PSf | 0.1167 | 1.603 | 88.3% |
| (B) Permeability depends on xGnP/PSf | 0.0223 | 2.360 | 97.8% |
| Permeability depends on Au/PSf | 0.2169 | -1.251 | 78.3% |
| (C) $k_{obs} \cdot \ell_{eff}$ depends on Au/PSf | 4.61E-06 | 5.274 | 100.0% |
| (D) Permeability depends on xGnP/PSf | 0.0049 | 2.940 | 99.5% |

2.4.9 Practicability and environmental applications

The high cost of engineered nanomaterials is often the initial barrier for the translation of nano-enabled products to market and practice. Being significantly less expensive (\$0.13 per gram) than carbon nanotubes, xGnPs is a relatively low cost material. xGnP-supported catalysis can be a cost-effective treatment alternative for difficult to remove chemicals such as chlorinated organics, nitrate, nitrite, and perchlorate. These compounds are all subject to EPA national primary drinking water regulations as contaminants that pose human health risks.

Activated carbon adsorption, ion exchange, and reverse osmosis, which are the currently practiced treatment methods for these pollutants, transfer the toxic compounds from one phase to another, so that the separated pollutants can be safely disposed. Reactive separations have the advantage of transforming pollutants to less toxic or nontoxic compounds obviating the need for concentrate disposal.

Coupling catalysis with membrane separation can enable further increases in reaction efficiency. Indeed, some of the most efficient reactive separations are performed using catalytic membrane reactors. Immobilizing catalysts and operating the process in a flow-through mode helps to overcome diffusion limitation, obviates the need to recover the catalysts, and minimizes the aggregation of the catalyst nanoparticles. When supported on high surface area “carrier” nanoparticles such as xGnPs, nanocatalysts can be more efficiently

utilized because of the better dispersion along the support surface (minimal aggregation) and throughout the membrane.

Extending the proposed concept to the case of 3 hierarchy levels, graphene-based materials can support and “deliver” bimetallic catalysts that are especially promising as they enable very high reactions rates [46]. When using Pd-on-Au nanocatalyst for the hydrodechlorination of trichloroethylene, significantly higher reaction rate constants were observed and catalyst poisoning, typical for monometallic Pd catalysts, was eliminated [47]. Pd-Cu nanocatalyst can be used in the reduction of both nitrate and nitrite, where Cu acts as a promoter metal in for the catalytic reduction of nitrate species [48]. Carbon supported Re-Pd catalysts displayed catalytic activity for the reduction of perchlorate in water [49].

Using more effective catalysts such as those mentioned above can help to address the challenge inherent to flow-through membrane reactors - the conflicting requirements of the higher product water flux and higher treatment efficiency. At higher permeate fluxes the residence time of a pollutant in the membrane reactor is smaller leading to lesser treatment efficiency. **Figure 13** illustrates the decrease of % reduction of 4-NP with an increase in treated water flux. Finally, anchoring smaller NPs to the larger carrier NPs such as xGnPs can minimize NP loss from various nano-enabled materials such as water treatment membranes where the NP release can be facilitated by the permeate flow.

To scale up the lab-based procedure for fabricating Au-xGnP nanocomposite membranes, a modified approach to decorate xGnP would be needed to achieve cost-effective production. The decoration method used in this study only produced small amounts (~400 mg per batch) of Au-xGnP. One method that might prove scalable would be to functionalize the xGnP and simply add the gold precursor and borohydride as a reducing agent for the gold precursor while stirring.

2.5 Conclusions

Hierarchical functional nanostructures are proposed as “building blocks” for the design of multifunctional membranes. Exfoliated graphite nanoplatelets (xGnPs) decorated by Au nanoparticles were added to the PSf-NMP-PEG casting mixtures prior to forming nanocomposite membranes by phase inversion. The nanocomposite membranes with only 1% xGnP loading were on average 9 times more resistant to compaction, 70 times more permeable, and had 2 times higher rejection than xGnP-free membranes. The structure and catalytic activity of such membranes could be controlled separately by regulating the relative content of components representing different levels in the nanofiller hierarchy. Specifically, by mixing Au-decorated xGnPs and Au-free xGnPs in different relative amounts and adding the resulting mixtures to the membrane, the structure (controlled by the total amount of xGnPs) and reactivity (controlled by the total surface area of gold nanoparticles) could be controlled almost independently. The design concept can be expanded to involve alternative supports, other functional NPs, or nanofillers with higher hierarchy levels. For example, bimetallic catalysts supported on xGnPs could be used to enhance environmentally important catalytic reactions such as denitrification, dehalogenation, and perchlorate removal.

Acknowledgements

This work was supported by the Paul L. Bush award from the Water Environment Research Foundation, the NSF Partnerships for International Education and Research grant OISE-0530174, and a Strategic Partnership grant from the MSU Foundation. We thank Mr. Nathaniel Danforth for his help with the preparation of gold-decorated xGnPs and Ms. Elodie Pasco for useful discussions. ARR also acknowledges North American Membrane Society for the support via the “International research internships: Membrane separations for water quality control” award and the American Water Works Association (Michigan section) for Water Quality and Treatment Study fellowship. Finally, we are grateful to XG Science, Inc. for donating xGnPs.

Supporting information for Chapter 2

S1. Characterization of permeability, catalytic reactivity, and selectivity

Permeability measurements, rejection studies, and filtration experiments were conducted with a transmembrane pressure of 20 psi. However, one 0.1% xGnP/PSf loading and two xGnP-free membranes were too dense to achieve sufficient flux at 20 psi. Therefore, the transmembrane pressure for these denser membranes was increased to 40 psi for permeability measurements and filtration experiments.

Membrane permeability and catalytic reactivity were characterized using the same experimental setup except that borohydride was a component in the 4-NP feed solution during the catalytic measurements and step pressures of 20, 16, 12, and 8 psi were used. **Figure 15** Figure 15 shows the schematic of the experimental unit used to measure permeability and catalytic reactivity. **Figure 16** show an example experimental data set. **Figure 17** shows an example of the reactive flux calculation and fit.

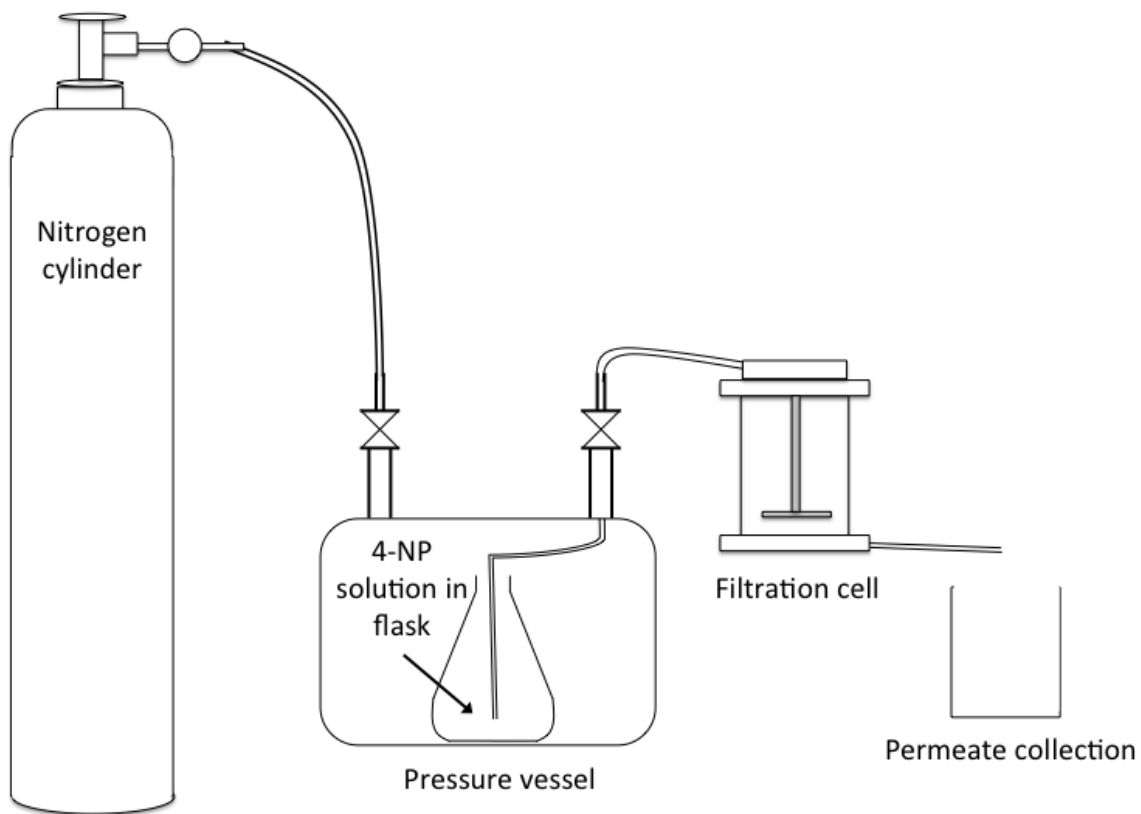


Figure 15: Schematic of experimental setup for permeability and catalytic measurements.

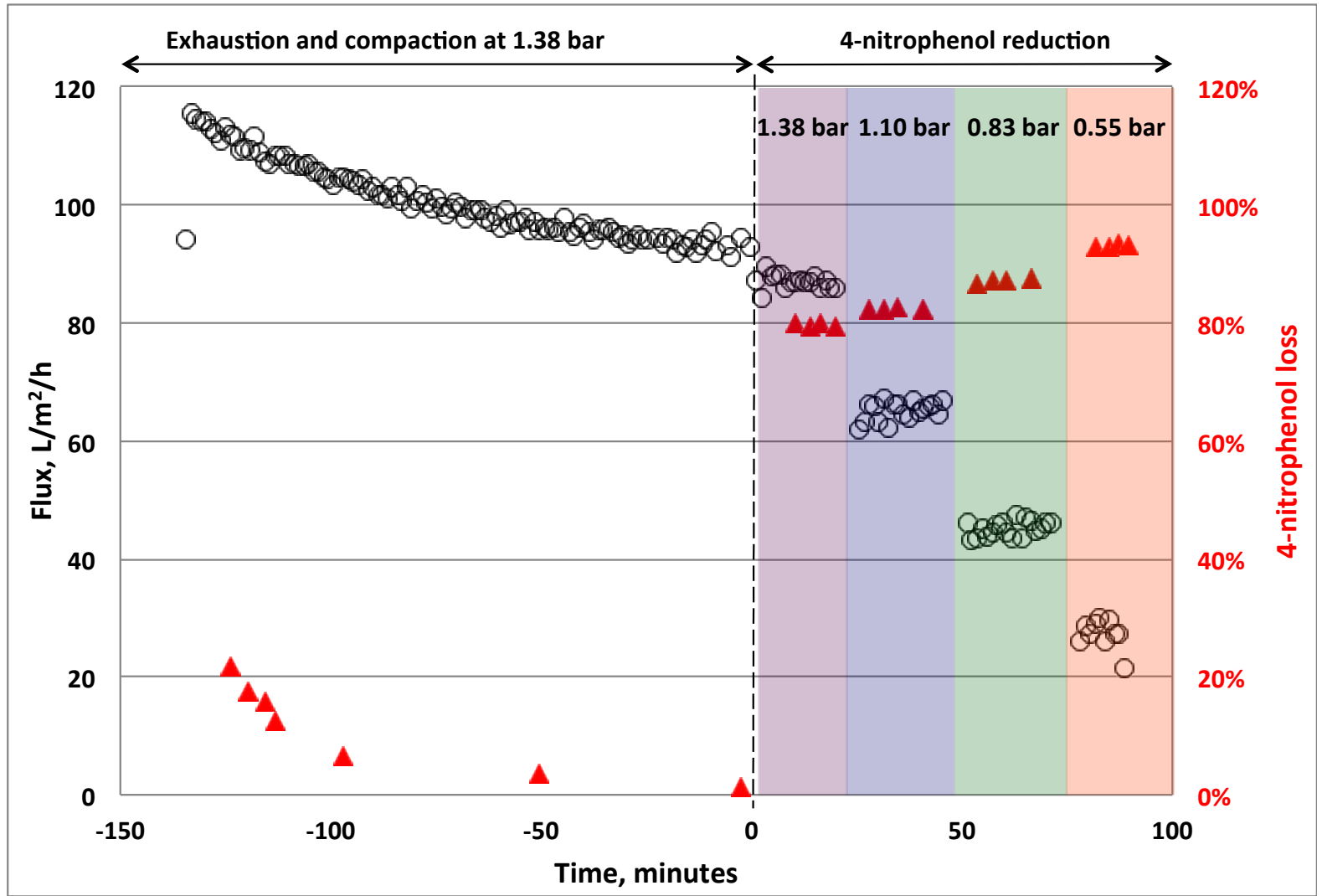


Figure 16: Permeate flux and 4-NP reduction as a function of time.

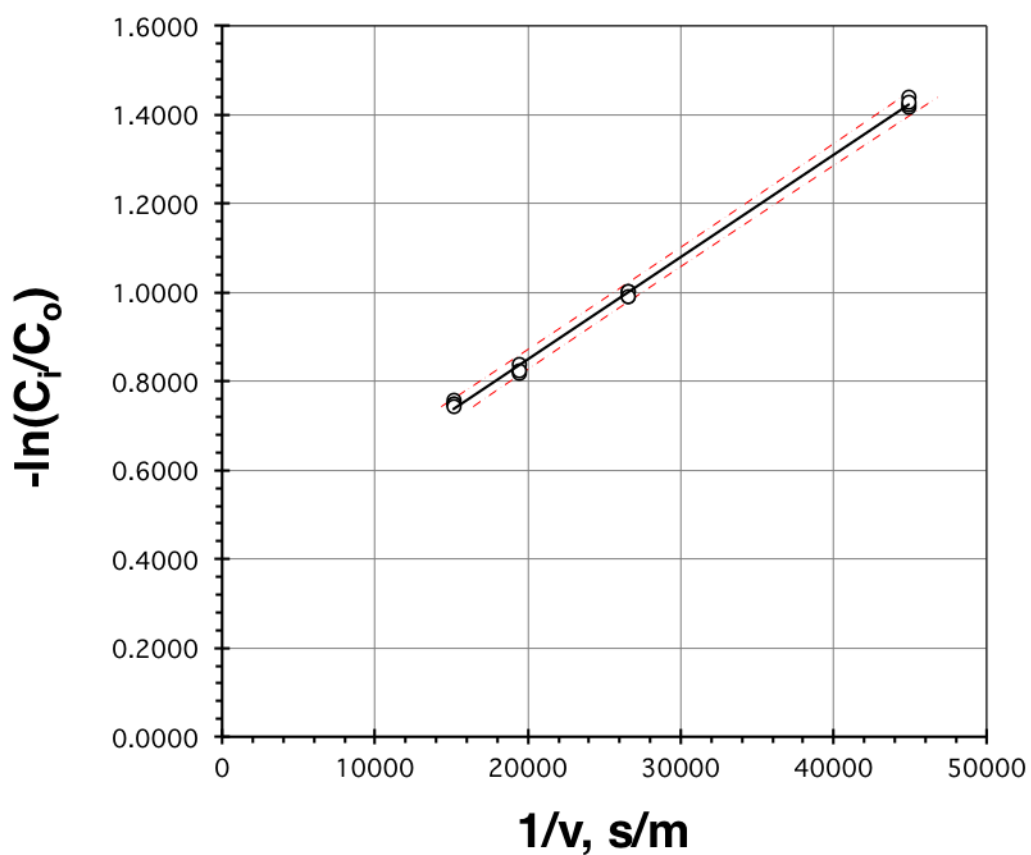


Figure 17: The figure shows an example fit as a pseudo plug reactor in the first order. For each flux four measurements of 4-nitrophenol reduction were used, and the red dashed line represents the 90% confidence interval of the fit.

For each cast membrane, 3 coupons were cutout where permeability, selectivity, reactivity, and mechanical properties were measured for each. **Figure 18** shows a schematic of how each cast membrane was divided into sections where specific coupons were cut for specific characterization experiments.

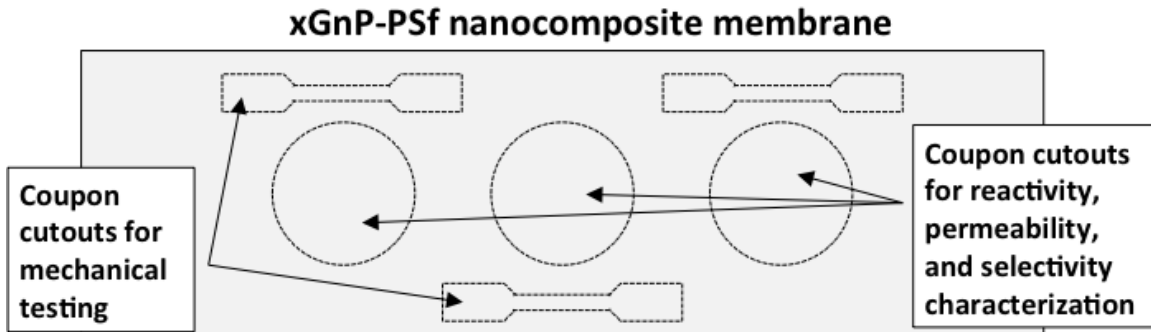


Figure 18: A schematic showing how the cast nanocomposite membrane was apportioned for specific characterization experiments.

For the calculation of the figure of merit (see **Figure 22**), 12 kDa dextran was used as a rejection probe, but other molecular weights of dextran were used in selectivity studies. **Table 3** shows the rejections of for nanocomposite membranes.

Table 3: The average rejection of dextrans with molecular weights, 5, 12, 25, 80, and 150 kDa are recorded in the table with the corresponding 90% confidence interval.

| Membrane | | Dextran rejection, % | | | | | | | | | |
|----------|-------------------|----------------------|-----------|-----------|-----------|-----------|-----------|-----------|-----------|------------|-----------|
| Name | xGnP/PS f, wt% | 5 kDa | 90% CI | 12 kDa | 90% CI | 25 kDa | 90% CI | 80 kDa | 90% CI | 150 kDa | 90% CI |
| A | 0 | 10.3% | 1.5% | 27.5% | 2.2% | 56.0% | 5.4% | 82.3% | 6.7% | 91.0% | 3.8% |
| B | 0.1 | 41.4% | 9.8% | 68.4% | 12.5% | 88.9% | 5.4% | 96.8% | 1.4% | 97.0% | 1.4% |
| C and C* | 0.5 | 43.5% | 13.2% | 69.7% | 11.3% | 87.3% | 6.3% | 95.6% | 1.7% | 97.1% | 1.1% |
| D and D* | 1 | 28.0% | 9.7% | 59.3% | 7.8% | 84.7% | 4.0% | 94.5% | 1.7% | 97.5% | 0.2% |
| E | 2 | 7.8% | 3.3% | 24.5% | 8.2% | 45.9% | 15.2% | 73.2% | 18.9% | 89.3% | 9.5% |

S2. Aggregation of gold nanoparticles on xGnP observed during preliminary studies

In preliminary studies of xGnP decoration, aggregation of gold NPs was observed. The size of aggregates in these preliminary studies was greater than 1 μ . **Figure 19** shows an SEM image of an xGnP with aggregated nanogold using. Following preliminary studies, the aggregation of gold NPs was overcome by using fresh solutions of NaOH during xGnP decoration – adequate dispersion of gold NPs in the range of 10 – 50 nm was confirmed by SEM (see **Figure 5**) during all following experiments.

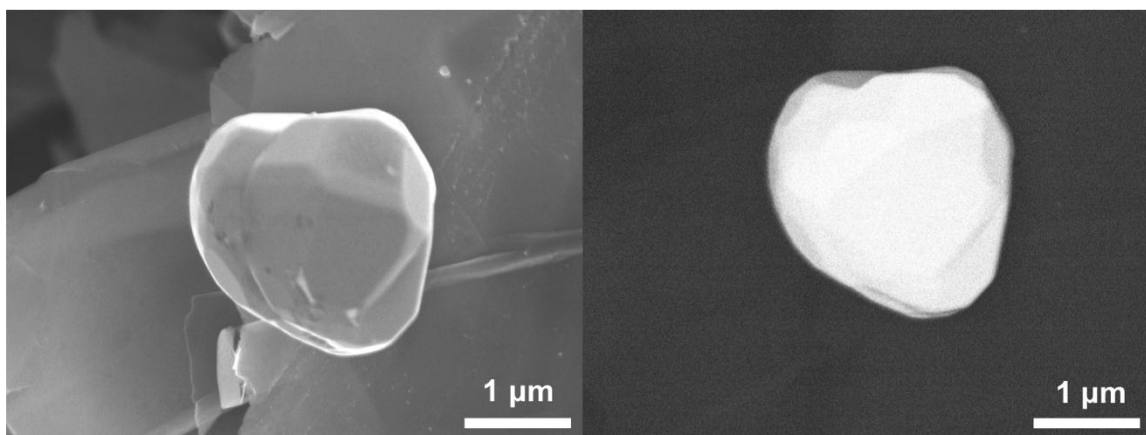


Figure 19: SEM micrographs of aggregated nanogold. The image was obtained using the backscatter electron detector (a) and secondary electron detector (b)

S3. Backscatter SEM micrographs and X-ray diffraction of Au-xGnPs

Backscatter electron SEM and X-ray diffraction were used to confirm that xGnPs were decorated with nanogold. **Figure 20** and **Figure 21** show the SEM micrograph and XRD data, respectively.

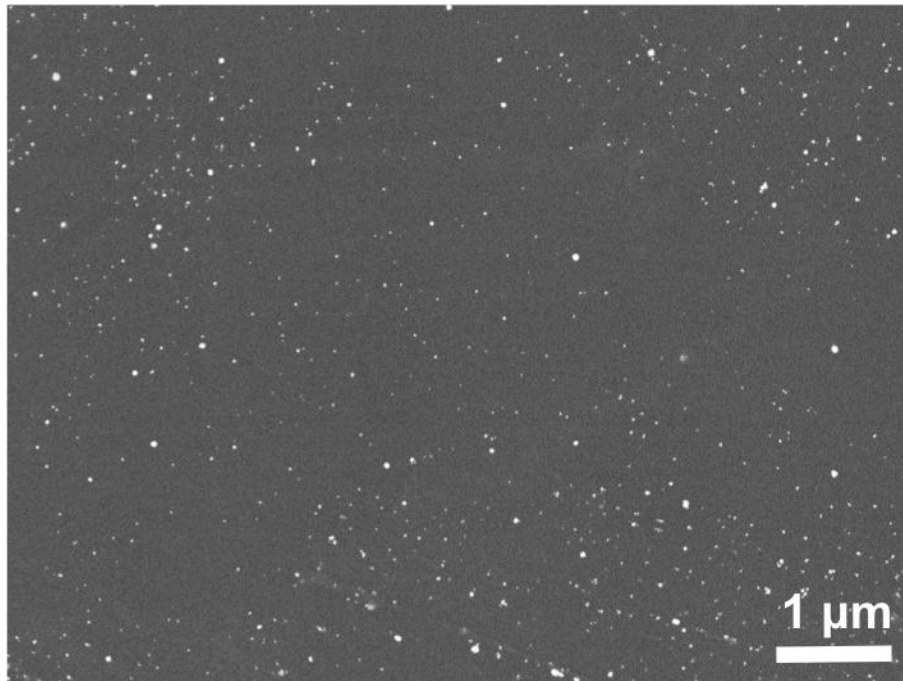


Figure 20: Backscatter SEM micrograph of Au-xGnP.

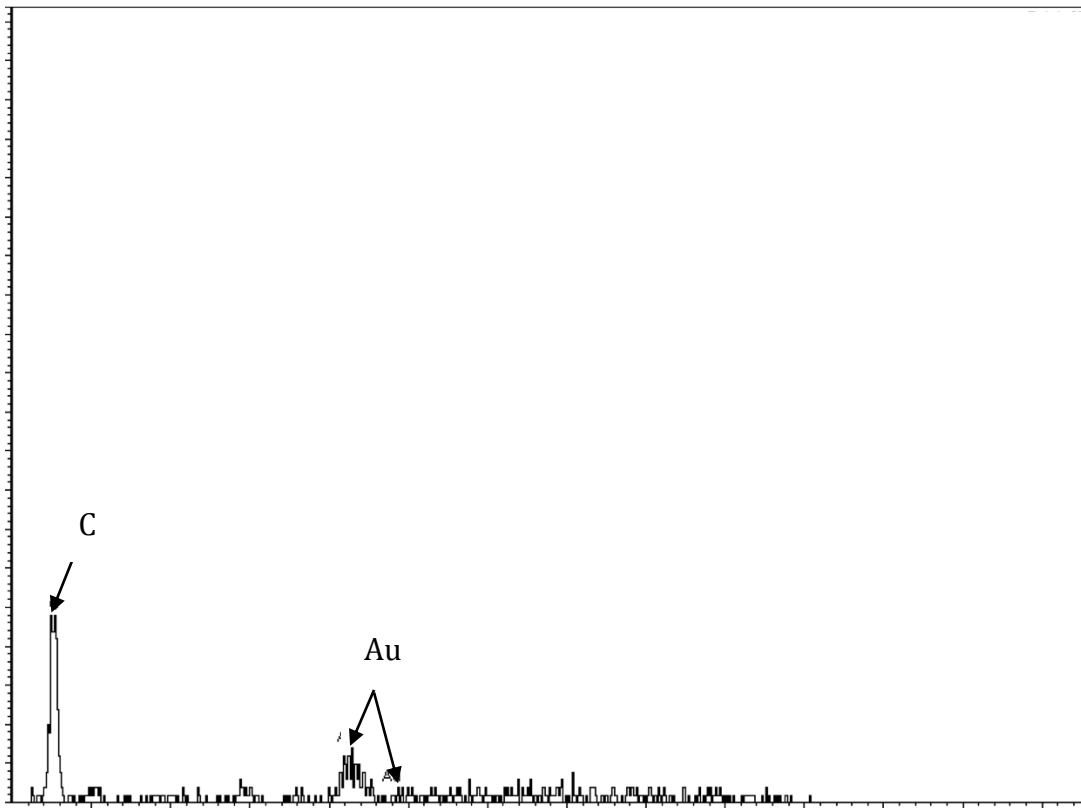


Figure 21: X-ray diffraction spectrum of Au-xGnP diffraction peaks corresponding to Au and C.

S4. Figure of merit

To characterize the overall performance of nanocomposite membranes, a figure of merit was determined by the rejection, using 12 kDa dextran as a rejection probe, and permeability of the membranes. **Figure 22** shows the figure of merit (Rejection, % \times Permeability, L/(m²-h-bar)) for nanocomposite membranes.

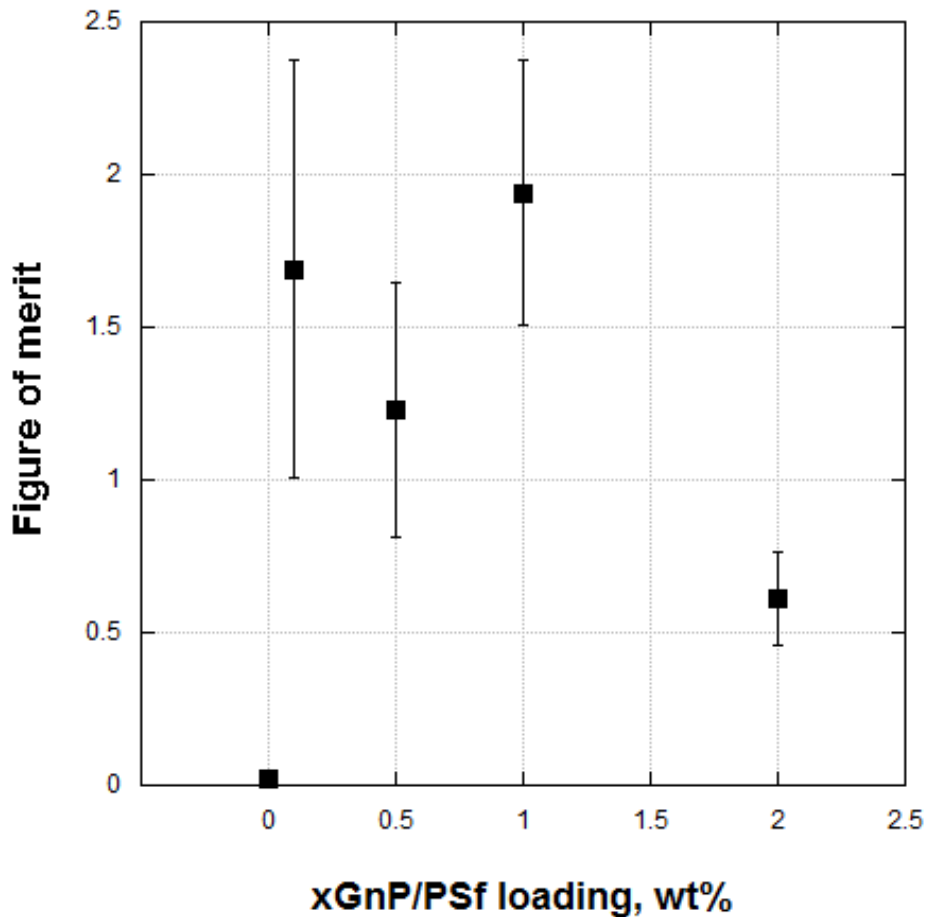


Figure 22: The figure of merit is calculated as permeability, L/(m²-h-bar) \times 12 kDa rejection, % and is plotted as a function of xGnP/PSf loading.

APPENDIX

APPENDIX

The following describes the plug flow model with a first order reaction (Section 2.4.6).

List of terms:

x = distance in reactor,

C = 4-NP concentration at a distance, x , from the reactor's inlet,

C_0 = initial or feed 4-NP concentration,

C_l = 4-NP concentration,

k_{obs} = observed reaction rate constant for the reduction of 4-NP,

l_{eff} = effective length of the plug flow reactor,

E = dispersion coefficient,

v = superficial velocity.

Advection-dispersion equation with a first order reaction in one dimension

$$\frac{\delta C}{\delta t} = E \left[\frac{\delta^2 C}{\delta x^2} \right] - v \frac{\delta C}{\delta x} - k_{obs} C \quad (1)$$

The concentration profile of 4-NP along the reactor's length was assumed to achieve steady state and not changing in time. This means that the partial derivative of concentration with respect to time is 0.

$$0 = E \left[\frac{d^2 C}{dx^2} \right] - v \frac{dC}{dx} - k_{obs} C \quad (2)$$

Assuming that the dispersion term is 0 gives:

$$0 = -v \frac{dC}{dx} - k_{obs} C$$

To solve the differential equation, the terms are separated and both sides of the equation are integrated.

$$-v \frac{dC}{dx} = k_{obs} C \quad (3)$$

$$\int \frac{1}{C} dC = -\frac{1}{v} k_{obs} \int dx$$

The boundary conditions for the concentration are from the feed concentration (C_0) to the effluent concentration (C_l) at effective length, l_{eff} . The boundary conditions for the distance, x , of the plug flow are from distance 0 to l_{eff} .

$$\ln[C]_{C_0}^{C_l} = -\frac{1}{v} k_{obs} \cdot x \Big|_0^{l_{eff}}$$

$$\ln \left[\frac{C_l}{C_0} \right] = -\frac{1}{v} k_{obs} \cdot l_{eff}$$

The solved equation describes steady state plug flow with a first order reaction with no dispersion.

$$C_l = C_0 \exp \left[-\frac{k_{obs}}{v} \cdot l_{eff} \right] \quad (4)$$

REFERENCES

REFERENCES

- [1] J. Kim and B. Van der Bruggen, "The use of nanoparticles in polymeric and ceramic membrane structures: Review of manufacturing procedures and performance improvement for water treatment," *Environmental Pollution*, vol. 158, no. 7, pp. 2335–2349, Jul. 2010.
- [2] M. M. Pendergast and E. M. V. Hoek, "A review of water treatment membrane nanotechnologies," *Energy Environ. Sci.*, vol. 4, no. 6, pp. 1946–1971, Jun. 2011.
- [3] P. Aerts, S. Kuypers, I. Genné, R. Leysen, J. Mewis, I. F. J. Vankelecom, and P. A. Jacobs, "Polysulfone–ZrO₂ Surface Interactions. The Influence on Formation, Morphology and Properties of Zirfon-Membranes," *J. Phys. Chem. B*, vol. 110, no. 14, pp. 7425–7430, 2006.
- [4] B. J. Hinds, N. Chopra, T. Rantell, R. Andrews, V. Gavalas, and L. G. Bachas, "Aligned multiwalled carbon nanotube membranes," *Science*, vol. 303, no. 5654, pp. 62–65, Jan. 2004.
- [5] J. S. Taurozzi, H. Arul, V. Z. Bosak, A. F. Burban, T. C. Voice, M. L. Bruening, and V. V. Tarabara, "Effect of filler incorporation route on the properties of polysulfone-silver nanocomposite membranes of different porosities," *Journal of Membrane Science*, vol. 325, no. 1, pp. 58–68, Nov. 2008.
- [6] L. Qiu, X. Zhang, W. Yang, Y. Wang, G. P. Simon, and D. Li, "Controllable corrugation of chemically converted graphene sheets in water and potential application for nanofiltration," *Chem. Commun.*, vol. 47, no. 20, pp. 5810–5812, May 2011.
- [7] S. J. Chae, F. Güneş, K. K. Kim, E. S. Kim, G. H. Han, S. M. Kim, H.-J. Shin, S.-M. Yoon, J.-Y. Choi, M. H. Park, C. W. Yang, D. Pribat, and Y. H. Lee, "Synthesis of Large-Area Graphene Layers on Poly-Nickel Substrate by Chemical Vapor Deposition: Wrinkle Formation," *Advanced Materials*, vol. 21, no. 22, pp. 2328–2333, 2009.
- [8] R. R. Nair, H. A. Wu, P. N. Jayaram, I. V. Grigorieva, and A. K. Geim, "Unimpeded Permeation of Water Through Helium-Leak-Tight Graphene-Based Membranes," *Science*, vol. 335, no. 6067, pp. 442–444, Jan. 2012.
- [9] A. Tiraferri, C. D. Vecitis, and M. Elimelech, "Covalent Binding of Single-Walled Carbon Nanotubes to Polyamide Membranes for Antimicrobial Surface Properties," *ACS Applied Materials & Interfaces*.
- [10] B. H. Jeong, E. Hoek, Y. Yan, A. Subramani, X. Huang, G. Hurwitz, A. K. Ghosh, and A. Jawor, "Interfacial polymerization of thin film nanocomposites: A new concept for reverse osmosis membranes," *Journal of Membrane Science*, vol. 294, no. 1, pp. 1–7, 2007.

- [11] K. Zodrow, L. Brunet, S. Mahendra, D. Li, A. Zhang, Q. Li, and P. J. J. Alvarez, "Polysulfone ultrafiltration membranes impregnated with silver nanoparticles show improved biofouling resistance and virus removal," *Water Research*, vol. 43, no. 3, pp. 715–723, Feb. 2009.
- [12] V. V. Tarabara, "Multifunctional nanomaterial-enabled membranes for water treatment," *Nanotechnology Applications for Clean Water*, William Andrew Inc, pp. 59–75, 2009.
- [13] S. R. Lewis, S. Datta, M. Gui, E. L. Coker, F. E. Huggins, S. Daunert, L. Bachas, and D. Bhattacharyya, "Reactive nanostructured membranes for water purification," *PNAS*, May 2011.
- [14] B. Schlichter, V. Mavrov, and H. Chmiel, "Study of a hybrid process combining ozonation and microfiltration/ultrafiltration for drinking water production from surface water," *Desalination*, vol. 168, no. 0, pp. 307–317, Aug. 2004.
- [15] B. S. Karnik, S. H. R. Davies, K. C. Chen, D. R. Jaglowski, M. J. Baumann, and S. J. Masten, "Effects of ozonation on the permeate flux of nanocrystalline ceramic membranes," *Water Research*, vol. 39, no. 4, pp. 728–734, Feb. 2005.
- [16] J. Dai and M. L. Bruening, "Catalytic Nanoparticles Formed by Reduction of Metal Ions in Multilayered Polyelectrolyte Films," *Nano Lett.*, vol. 2, no. 5, pp. 497–501, 2002.
- [17] D. M. Dotzauer, J. Dai, L. Sun, and M. L. Bruening, "Catalytic Membranes Prepared Using Layer-by-Layer Adsorption of Polyelectrolyte/Metal Nanoparticle Films in Porous Supports," *Nano Lett.*, vol. 6, no. 10, pp. 2268–2272, 2006.
- [18] H. Choi, A. C. Sofranko, and D. D. Dionysiou, "Nanocrystalline TiO₂ Photocatalytic Membranes with a Hierarchical Mesoporous Multilayer Structure: Synthesis, Characterization, and Multifunction," *Advanced Functional Materials*, vol. 16, no. 8, pp. 1067–1074, 2006.
- [19] J. Xu and D. Bhattacharyya, "Fe/Pd Nanoparticle Immobilization in Microfiltration Membrane Pores: Synthesis, Characterization, and Application in the Dechlorination of Polychlorinated Biphenyls," *Ind. Eng. Chem. Res.*, vol. 46, no. 8, pp. 2348–2359, 2006.
- [20] P. Aerts, I. Genne, S. Kuypers, R. Leysen, I. F. . Vankelecom, and P. . Jacobs, "Polysulfone–aerosil composite membranes: Part 2. The influence of the addition of aerosil on the skin characteristics and membrane properties," *Journal of Membrane Science*, vol. 178, no. 1–2, pp. 1–11, Sep. 2000.
- [21] J. S. Taurozzi, C. A. Crock, and V. V. Tarabara, "C60-polysulfone nanocomposite membranes: Entropic and enthalpic determinants of C60 aggregation and its effects on membrane properties," *Desalination*, vol. 269, no. 1–3, pp. 111–119, Mar. 2011.

- [22] L. Brunet, D. Y. Lyon, K. Zodrow, J.-C. Rouch, B. Caussat, P. Serp, J.-C. Remigy, M. R. Wiesner, and P. J. J. Alvarez, "Properties of Membranes Containing Semi-dispersed Carbon Nanotubes," *Environmental Engineering Science*, vol. 25, no. 4, pp. 565–576, May 2008.
- [23] P. V. Kamat, "Graphene-Based Nanoarchitectures. Anchoring Semiconductor and Metal Nanoparticles on a Two-Dimensional Carbon Support," *The Journal of Physical Chemistry Letters*, vol. 1, no. 2, pp. 520–527, Jan. 2010.
- [24] V. Singh, D. Joung, L. Zhai, S. Das, S. I. Khondaker, and S. Seal, "Graphene based materials: Past, present and future," *Progress in Materials Science*, vol. 56, no. 8, pp. 1178–1271, Oct. 2011.
- [25] C. Xu, X. Wang, and J. Zhu, "Graphene–Metal Particle Nanocomposites," *J. Phys. Chem. C*, vol. 112, no. 50, pp. 19841–19845, 2008.
- [26] K. Kalaitzidou, H. Fukushima, and L. T. Drzal, "Mechanical properties and morphological characterization of exfoliated graphite–polypropylene nanocomposites," *Composites Part A: Applied Science and Manufacturing*, vol. 38, no. 7, pp. 1675–1682, Jul. 2007.
- [27] F. Fievet, J. P. Lagier, B. Blin, B. Beaudoin, and M. Figlarz, "Homogeneous and heterogeneous nucleations in the polyol process for the preparation of micron and submicron size metal particles," *Solid State Ionics*, vol. 32–33, no. Part 1, pp. 198–205, February.
- [28] W. Li, C. Liang, W. Zhou, J. Qiu, Zhou, G. Sun, and Q. Xin, "Preparation and Characterization of Multiwalled Carbon Nanotube-Supported Platinum for Cathode Catalysts of Direct Methanol Fuel Cells," *The Journal of Physical Chemistry B*, vol. 107, no. 26, pp. 6292–6299, Jul. 2003.
- [29] C. C. Li, W. P. Cai, B. Q. Cao, F. Q. Sun, Y. Li, C. X. Kan, and L. D. Zhang, "Mass Synthesis of Large, Single-Crystal Au Nanosheets Based on a Polyol Process," *Adv. Funct. Mater.*, vol. 16, no. 1, pp. 83–90, Jan. 2006.
- [30] C. Li, K. L. Shuford, M. Chen, E. J. Lee, and S. O. Cho, "A Facile Polyol Route to Uniform Gold Octahedra with Tailorable Size and Their Optical Properties," *ACS Nano*, vol. 2, no. 9, pp. 1760–1769, 2008.
- [31] Q. Li, S. Mahendra, D. Y. Lyon, L. Brunet, M. V. Liga, D. Li, and P. J. J. Alvarez, "Antimicrobial nanomaterials for water disinfection and microbial control: Potential applications and implications," *Water Research*, vol. 42, no. 18, pp. 4591–4602, Nov. 2008.
- [32] S. Panigrahi, S. Basu, S. Praharaj, S. Pande, S. Jana, A. Pal, S. K. Ghosh, and T. Pal, "Synthesis and Size-Selective Catalysis by Supported Gold Nanoparticles: Study on Heterogeneous and Homogeneous Catalytic Process," *J. Phys. Chem. C*, vol. 111, no. 12, pp. 4596–4605, 2007.
- [33] M. Schrunner, F. Polzer, Y. Mei, Y. Lu, B. Haupt, M. Ballauff, A. Gödel, M. Drechsler, J. Preussner, and U. Glatzel, "Mechanism of the Formation of Amorphous Gold Nanoparticles within Spherical Polyelectrolyte Brushes,"

Macromolecular Chemistry and Physics, vol. 208, no. 14, pp. 1542–1547, 2007.

- [34] J. Lu, I. Do, L. T. Drzal, R. M. Worden, and I. Lee, “Nanometal-Decorated Exfoliated Graphite Nanoplatelet Based Glucose Biosensors with High Sensitivity and Fast Response,” *ACS Nano*, vol. 2, no. 9, pp. 1825–1832, 2008.
- [35] J. Wan, W. Cai, J. Feng, X. Meng, and E. Liu, “In situ decoration of carbon nanotubes with nearly monodisperse magnetite nanoparticles in liquid polyols,” *J. Mater. Chem.*, vol. 17, no. 12, p. 1188, 2007.
- [36] I.-H. Do, *Metal Decoration of Exfoliated Graphite Nanoplatelets (xGnP) for Fuel Cell Application*. ProQuest, 2006.
- [37] C. . Leon y Leon, J. . Solar, V. Calemma, and L. . Radovic, “Evidence for the protonation of basal plane sites on carbon,” *Carbon*, vol. 30, no. 5, pp. 797–811, 1992.
- [38] E. Antolini, “Formation, microstructural characteristics and stability of carbon supported platinum catalysts for low temperature fuel cells,” *Journal of materials science*, vol. 38, no. 14, pp. 2995–3005, 2003.
- [39] S. Wang, Y. Zhang, N. Abidi, and L. Cabrales, “Wettability and Surface Free Energy of Graphene Films,” *Langmuir*, vol. 25, no. 18, pp. 11078–11081, 2009.
- [40] K. Ebert, D. Fritsch, J. Koll, and C. Tjahjawiguna, “Influence of inorganic fillers on the compaction behaviour of porous polymer based membranes,” *Journal of Membrane Science*, vol. 233, no. 1–2, pp. 71–78, Apr. 2004.
- [41] T. Ramanathan, A. A. Abdala, S. Stankovich, D. A. Dikin, M. Herrera-Alonso, R. D. Piner, D. H. Adamson, H. C. Schniepp, X. Chen, R. S. Ruoff, S. T. Nguyen, I. A. Aksay, R. K. Prud’homme, and L. C. Brinson, “Functionalized graphene sheets for polymer nanocomposites,” *Nat. Nanotechnol.*, vol. 3, no. 6, pp. 327–331, Jun. 2008.
- [42] D. Cho, S. Lee, G. Yang, H. Fukushima, and L. T. Drzal, “Dynamic Mechanical and Thermal Properties of Phenylethynyl-Terminated Polyimide Composites Reinforced With Expanded Graphite Nanoplatelets,” *Macromolecular Materials and Engineering*, vol. 290, no. 3, pp. 179–187, Mar. 2005.
- [43] K. M. Persson, V. Gekas, and G. Trägårdh, “Study of membrane compaction and its influence on ultrafiltration water permeability,” *Journal of Membrane Science*, vol. 100, no. 2, pp. 155–162, Apr. 1995.
- [44] M. T. M. Pendergast, J. M. Nygaard, A. K. Ghosh, and E. M. V. Hoek, “Using nanocomposite materials technology to understand and control reverse osmosis membrane compaction,” *Desalination*, vol. 261, no. 3, pp. 255–263, Oct. 2010.

- [45] N. Pradhan, A. Pal, and T. Pal, "Silver nanoparticle catalyzed reduction of aromatic nitro compounds," *Colloids and Surfaces A: Physicochemical and Engineering Aspects*, vol. 196, no. 2–3, pp. 247–257, Jan. 2002.
- [46] M. S. Wong, P. J. J. Alvarez, Y. Fang, N. Akçin, M. O. Nutt, J. T. Miller, and K. N. Heck, "Cleaner water using bimetallic nanoparticle catalysts," *Journal of Chemical Technology & Biotechnology*, vol. 84, no. 2, pp. 158–166, 2009.
- [47] M. O. Nutt, J. B. Hughes, and M. S. Wong, "Designing Pd-on-Au Bimetallic Nanoparticle Catalysts for Trichloroethene Hydrodechlorination," *Environ. Sci. Technol.*, vol. 39, no. 5, pp. 1346–1353, 2005.
- [48] U. Prüsse and K.-D. Vorlop, "Supported bimetallic palladium catalysts for water-phase nitrate reduction," *Journal of Molecular Catalysis A: Chemical*, vol. 173, no. 1–2, pp. 313–328, Sep. 2001.
- [49] Y. Zhang, K. D. Hurley, and J. R. Shapley, "Heterogeneous Catalytic Reduction of Perchlorate in Water with Re–Pd/C Catalysts Derived from an Oxorhenium(V) Molecular Precursor," *Inorg. Chem.*, vol. 50, no. 4, pp. 1534–1543, 2011.